Article

Molecular Cell

RNase L Reprograms Translation by Widespread mRNA Turnover Escaped by Antiviral mRNAs

Graphical Abstract

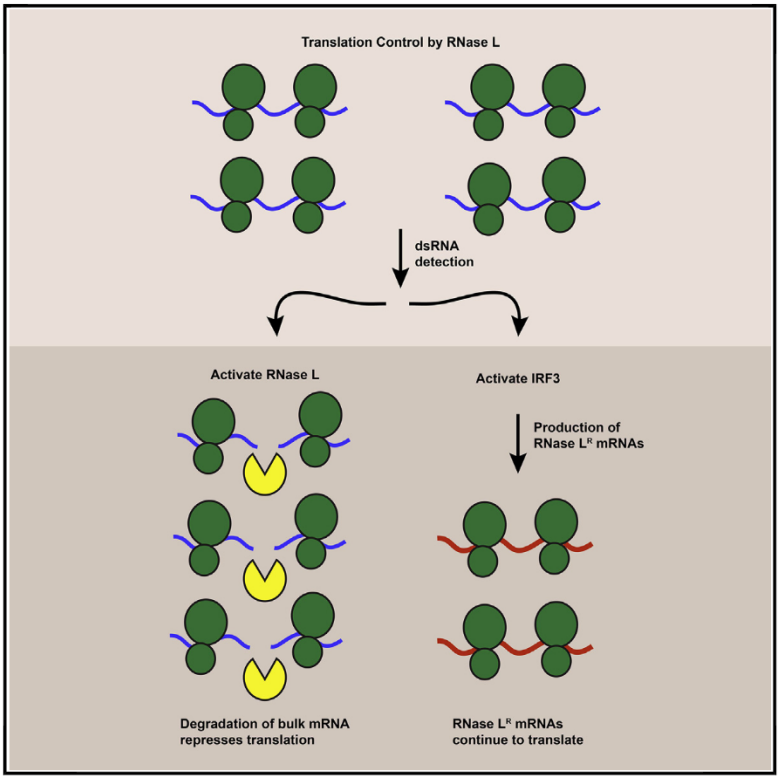

Authors

James M. Burke, Stephanie L. Moon, Tyler Matheny, Roy Parker

Correspondence

roy.parker@colorado.edu

In Brief

Burke et al. demonstrate that RNase L reduces bulk translation and stress granule assembly in response to dsRNA via rapid and widespread decay of basal mRNAs. In contrast to basal mRNAs, antiviral mRNAs escape RNase L-mediated mRNA decay, which permits their translation during RNase L-mediated host shutoff.

Highlights

- RNase L promotes rapid and widespread decay of basal mRNAs
- RNase L limits SG assembly via turnover of SG-associated mRNAs
- Degradation of mRNAs accounts for RNase L-mediated shutoff of translation
- Antiviral mRNAs escape RNase L, permitting their translation during host shutoff

Burke et al., 2019, Molecular Cell *75*, 1203–1217
September 19, 2019
https://doi.org/10.1016/j.molcel.2019.07.029

CellPress

Molecular Cell
Article

CellPress

RNase L Reprograms Translation by Widespread mRNA Turnover Escaped by Antiviral mRNAs

James M. Burke,[1] Stephanie L. Moon,[1] Tyler Matheny,[1] and Roy Parker[1,2,3,*]
[1]Department of Chemistry and Biochemistry, University of Colorado, Boulder, CO 80309, USA
[2]Howard Hughes Medical Institute, University of Colorado, Boulder, CO 80309, USA
[3]Lead Contact
*Correspondence: roy.parker@colorado.edu
https://doi.org/10.1016/j.molcel.2019.07.029

SUMMARY

In response to foreign and endogenous double-stranded RNA (dsRNA), protein kinase R (PKR) and ribonuclease L (RNase L) reprogram translation in mammalian cells. PKR inhibits translation initiation through eIF2α phosphorylation, which triggers stress granule (SG) formation and promotes translation of stress responsive mRNAs. The mechanisms of RNase L-driven translation repression, its contribution to SG assembly, and its regulation of dsRNA stress-induced mRNAs are unknown. We demonstrate that RNase L drives translational shut-off in response to dsRNA by promoting widespread turnover of mRNAs. This alters stress granule assembly and reprograms translation by allowing translation of mRNAs resistant to RNase L degradation, including numerous antiviral mRNAs such as interferon (*IFN*)-β. Individual cells differentially activate dsRNA responses revealing variation that can affect cellular outcomes. This identifies bulk mRNA degradation and the resistance of antiviral mRNAs as the mechanism by which RNase L reprograms translation in response to dsRNA.

INTRODUCTION

Double-stranded RNA (dsRNA) is a viral pathogen-associated molecular pattern (PAMP) that can initiate the innate immune response (Jensen and Thomsen, 2012). Endogenous "self" dsRNAs can also initiate the innate immune response, and dysregulation of cellular pathways that reduce self-dsRNA causes human diseases, such as Aicardi-Goutières syndrome (AGS) (Pestal et al., 2015; Liddicoat et al., 2015; Li et al., 2017). Elevated levels of endogenous dsRNAs may also contribute to neurodegenerative diseases, such as ALS (Saldi et al., 2014; Krug et al., 2017) and can contribute to chronic inflammation associated with cancers and autoimmune disorders (Grivennikov et al., 2010; Waldner 2009).

Several pattern recognition receptors (PRRs) recognize dsRNA in mammalian cells (Jensen and Thomsen, 2012). Recognition of dsRNA by RIG-I, MDA-5, or TLR3 activates the transcription factors IRF3 and/or IRF7 thereby inducing type-1 interferons (IFNs) and inflammatory cytokines, which prime the antiviral state of cells (Ivashkiv and Donlin, 2014). Concurrent with the induction of antiviral genes, global translation is reduced by protein kinase R (PKR) and ribonuclease L (RNase L) to promote an antiviral cellular state that limits viral gene expression and transforms the functional cellular transcriptome, a process termed host shutoff (Iordanov et al., 2000).

Activation of PKR by dsRNA results in phosphorylation of eIF2α on serine 51, which reduces canonical translation initiation and promotes the translation of stress response mRNAs that use non-canonical translation initiation (Dalet et al., 2015). This also triggers the formation of stress granules (SGs), conserved RNA-protein complexes that contain non-translating mRNAs, RNA-binding proteins—G3BP1, PABPC1, TIA1—and several key antiviral PRRs—OAS/RNase L, PKR, MDA-5, and RIG-I (García et al., 2006; Onomoto et al., 2012; Reineke et al., 2012; Yoo et al., 2014). Many viruses inhibit SG assembly, suggesting that SGs serve as antiviral signaling hubs and/or reduce viral replication through the sequestration of viral mRNAs/proteins (Lloyd, 2013). However, the disassembly of SGs via dephosphorylation of p-eIF2α by GADD34, which is induced by IRF3, has been proposed to promote translation of stress-induced antiviral mRNAs that are sequestered to SGs (Dalet et al., 2017). Thus, the mechanisms and functions of SG assembly/disassembly during the dsRNA/antiviral response remain unclear.

RNase L is an endonuclease activated by oligo(2′-5′A), which is produced when OAS proteins bind to dsRNA. RNase L cleaves single-stranded RNA (ssRNA) regions at UN^N sites in several types of RNAs, including small non-coding RNAs (Y-RNAs and tRNAs), rRNAs, and host/viral mRNAs (Andersen et al., 2009; Chakrabarti et al., 2011; Brennan-Laun et al., 2014; Donovan et al., 2017). These activities of RNase L reduce viral gene expression and replication, arrest global translation, and promote apoptosis (Zhou et al., 1997). RNase L is proposed to arrest translation by either cleavage of rRNA or production of RNA cleavage fragments that signal for translational arrest (Wreschner et al., 1981; Donovan et al., 2017). However, because these modes of translational arrest are presumably non-specific, a mystery in the field is how dsRNA-induced antiviral mRNAs would be translated during RNase L-driven translational arrest.

We present data demonstrating that RNase L promotes rapid and widespread degradation of cellular mRNAs in response to

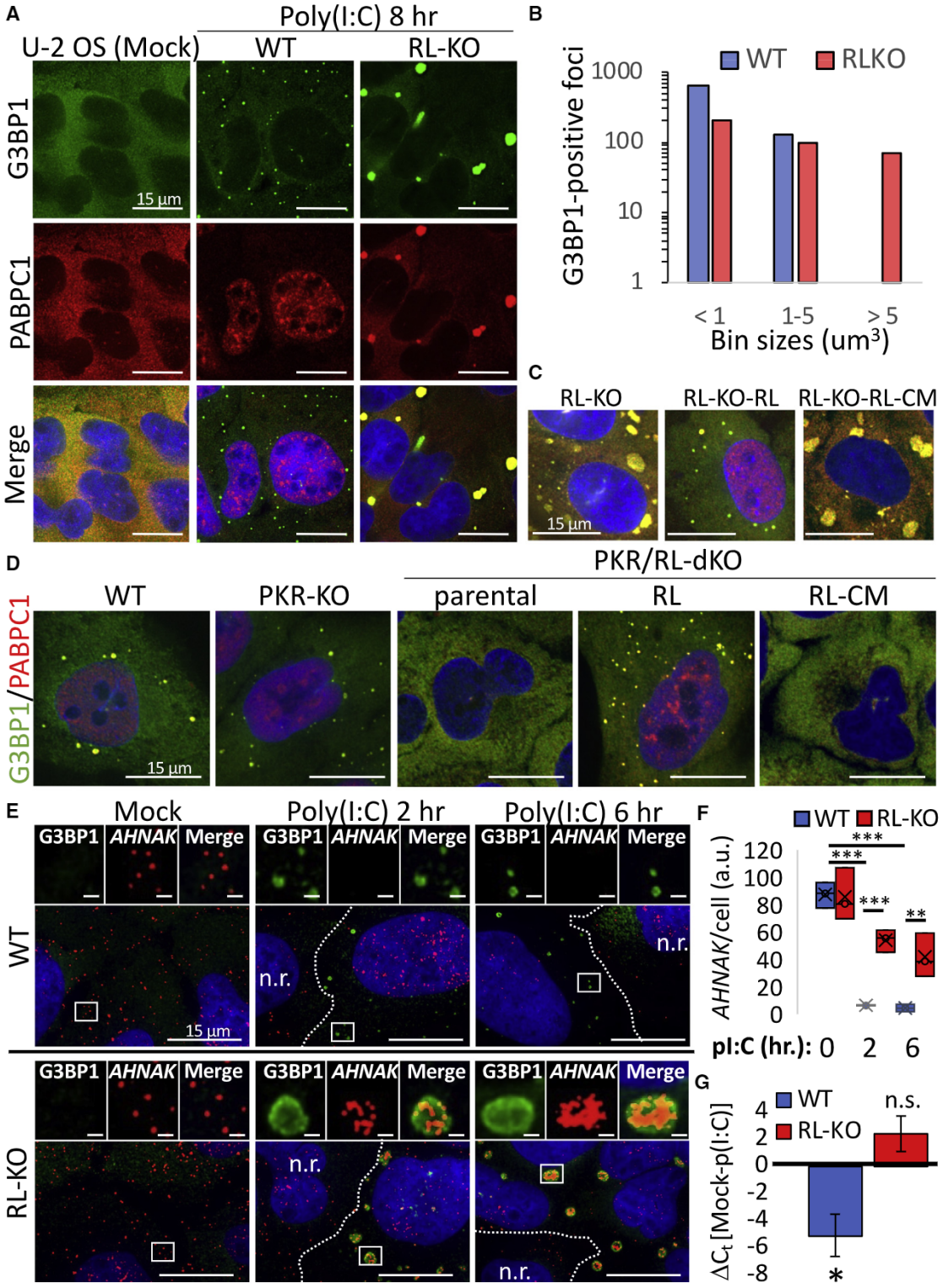

Figure 1. RNase L Catalytic Activity Alters SG Assembly and Reduces SG-Associated RNAs

(A) IF for SG-associated proteins G3BP1 and PABPC1 in WT and RL-KO U-2 OS cells.

(B) G3BP1-positive foci from >30 WT and RL-KO U-2 OS cells binned by volume.

(C) IF for G3BP1 and PABPC1 in parental RL-KO A549 cells stably expressing either RNase L (RL) or RNase L-R667A (RL-CM) 8 h post-poly(I:C). Images for G3BP1 and PABPC1 staining are shown in Figure S1E.

(legend continued on next page)

dsRNA, thus inhibiting SG assembly and decreasing translation. However, mRNAs encoding key antiviral proteins and cytokines, such as the *IFN-β* and interleukin (*IL*)*-6* mRNAs, escape RNase-L mediated mRNA turnover, which permits their translation during host shutoff when bulk mRNA turnover is the primary driver of global translation repression.

RESULTS

RNase L Catalytic Activity Alters SG Assembly and Reduces SG-Associated RNAs

RNase L represses translation and accumulates in stress granules (Onomoto et al., 2012; Reineke et al., 2012). Thus, we examined if RNase L activity affected stress granule assembly. We generated RNase L knockout (RL-KO) A549 and U-2 OS cell lines using CRISPR-Cas9 and then reconstituted expression of either RNase L or catalytically inactive RNase L-R667A in the RL-KO cells via lentiviral transduction or transient transfection (Figures S1A–S1C). Cells were transfected with high molecular weight poly(I:C), a viral dsRNA mimic that induces PKR-dependent SG assembly and activates the OAS/RNase L pathway. SG assembly was assessed by immunofluorescence assay (IF) for SG-associated proteins G3BP1 and PABPC1.

In comparison to the parental (wild type [WT]) cell lines, we observed two distinct phenotypes in RL-KO cell lines that were rescued by expression of RNase L, but not RNase L-R667A. First, SGs in the RL-KO cells were canonical in morphology (large and irregular in shape), whereas cytoplasmic puncta of G3BP1 and PABPC1 observed in the WT cells were invariably small and punctate (Figures 1A–1C, S1D, and S1E). Second, a substantial fraction of PABPC1 translocated from the cytosol to the nucleus in WT cells, whereas PABPC1 remained localized in the cytosol and SGs in RL-KO cells. The RNase L-dependent reduction in SG size was specific to the dsRNA stress response, as sodium arsenite treatment induced canonical SGs in both WT and RL-KO cells (Figure S1F). Moreover, the canonical dsRNA-induced SGs in RL-KO cells require PKR, whereas the small punctate dsRNA-induced SGs in WT cells are independent of PKR, but require RNase L catalytic activity (Figures 1D and S1G–S1J). We refer to these small punctate SGs in WT cells as RLBs (RNase L-dependent bodies) and use RLBs and nuclear PABP accumulation as markers for RNase L activation in subsequent single-cell analyses. These data indicate that RNase L activation alters SG assembly and instead leads to the assembly of RLBs.

Because mRNAs are an integral component of SGs (Van Treeck et al., 2018), and PABPC1 translocation to the nucleus occurs upon mRNA turnover (Lee and Glaunsinger, 2009; Kumar and Glaunsinger, 2010), we hypothesized that RNase L limits SG formation by degrading SG mRNAs. Single-molecule fluorescent *in situ* hybridization (smFISH) analysis of the SG-enriched *AHNAK* mRNA (Khong et al., 2017) revealed that this mRNA was strongly reduced in the cytosol and did not localize to RLBs in WT cells post-poly(I:C) (Figures 1E and 1F). In contrast, *AHNAK* mRNA remained abundant and localized to SGs in RL-KO cells. RT-qPCR analysis confirmed these results, showing that *AHNAK* mRNA levels significantly decreased in WT, but not RL-KO cells, post-poly(I:C) (Figure 1G). Analysis of the SG-enriched *NORAD* long non-coding RNA (lncRNA) yielded similar results (Figures S2A–S2C). These results demonstrate that RNase L alters SG assembly by degrading SG-associated RNAs.

RNase L Initiates Rapid and Widespread Turnover of mRNAs

We next examined whether RNase L affects mRNAs not enriched in SGs. The glyceraldehyde 3-phosphate dehydrogenase (*GAPDH*) mRNA, which is abundant and depleted from SGs (Khong et al., 2017), was reduced by at least 90% in the majority of WT A549 and U2-OS cells containing RLBs by 2 and 6 h post-poly(I:C) (Figures 2A, 2B, and S2D–S2F). Near complete reduction of *GAPDH* mRNA was observed in a fraction of A549 cells containing RLBs as early as 1-h post poly(I:C) (Figure S2G). In non-responsive neighboring cells (n.r.) that lack RLBs, *GAPDH* mRNA levels remained abundant and comparable to mock-treated cells. *GAPDH* mRNA levels were unchanged in RL-KO cells post-poly(I:C) (Figures 2A and 2B) and this was rescued by RNase L but not RNase L-R667A (Figures 2C and 2D), indicating that RNase L catalytic activity promotes *GAPDH* mRNA degradation. RT-qPCR analysis confirmed these observations, revealing that *GAPDH* mRNA levels, as well as *actin B* and *tubulin A* mRNAs, decreased (>75%) in WT but not RL-KO cells post-poly(I:C) (Figure 2E). Moreover, FISH for poly(A)$^+$ RNAs revealed at least a 70% RNase L-dependent decrease in cytosolic poly(A)$^+$ RNAs by 2 h post-poly(I:C) in cells containing RLBs (Figures 2F and 2G). These results suggest RNase L is degrading the majority of cytoplasmic mRNAs in response to dsRNA.

IFN-β and *IL-6* mRNAs Escape RNase L-Mediated mRNA Turnover

The degradation of host mRNAs by RNase L creates a problem for how cells undergoing the antiviral/dsRNA response produce proteins from IRF3-induced genes, such as IFN-β. Our smFISH/IF analyses revealed that not all cells activate RNase L-mediated mRNA decay (Figures 2 and S2F). Thus, one possibility is that antiviral mRNAs are degraded in cells that activate RNase L-mediated mRNA decay but are increased in cells not undergoing RNase L responses. Alternatively, IRF3-induced mRNAs may escape RNase L-dependent turnover. To test the latter hypothesis, we performed smFISH for the *IFN-β* mRNA simultaneously with the *GAPDH* mRNA to determine if *IFN-β* mRNAs were

(D) G3BP1 and PABPC1 IF in PKR-KO and PKR and RNase L double KO (PKR/RL-KO) A549 cells rescued with RNase L (RL) or RNase L-R667A (RL-CM) 6 h post-poly(I:C).

(E) smFISH for *AHNAK* mRNA in WT and RL-KO U-2 OS cells ± poly(I:C) with G3BP1 as a RLBs/SG marker. n.r., non-responsive cells with respect to RLB/SG assembly.

(F) Quantification of *AHNAK* mRNA smFISH from (E), with analysis of 17–30 RLB/SG+ cells in three fields of view.

(G) RT-qPCR analysis of AHNAK mRNA in WT and RL-KO A549 cells at 0 and 6 h post-poly(I:C) transfection. Bars represent the average Ct value differential ± SEM. from five independent experiments. Asterisk (*) indicates p value <0.05 as determined by Student's t test.

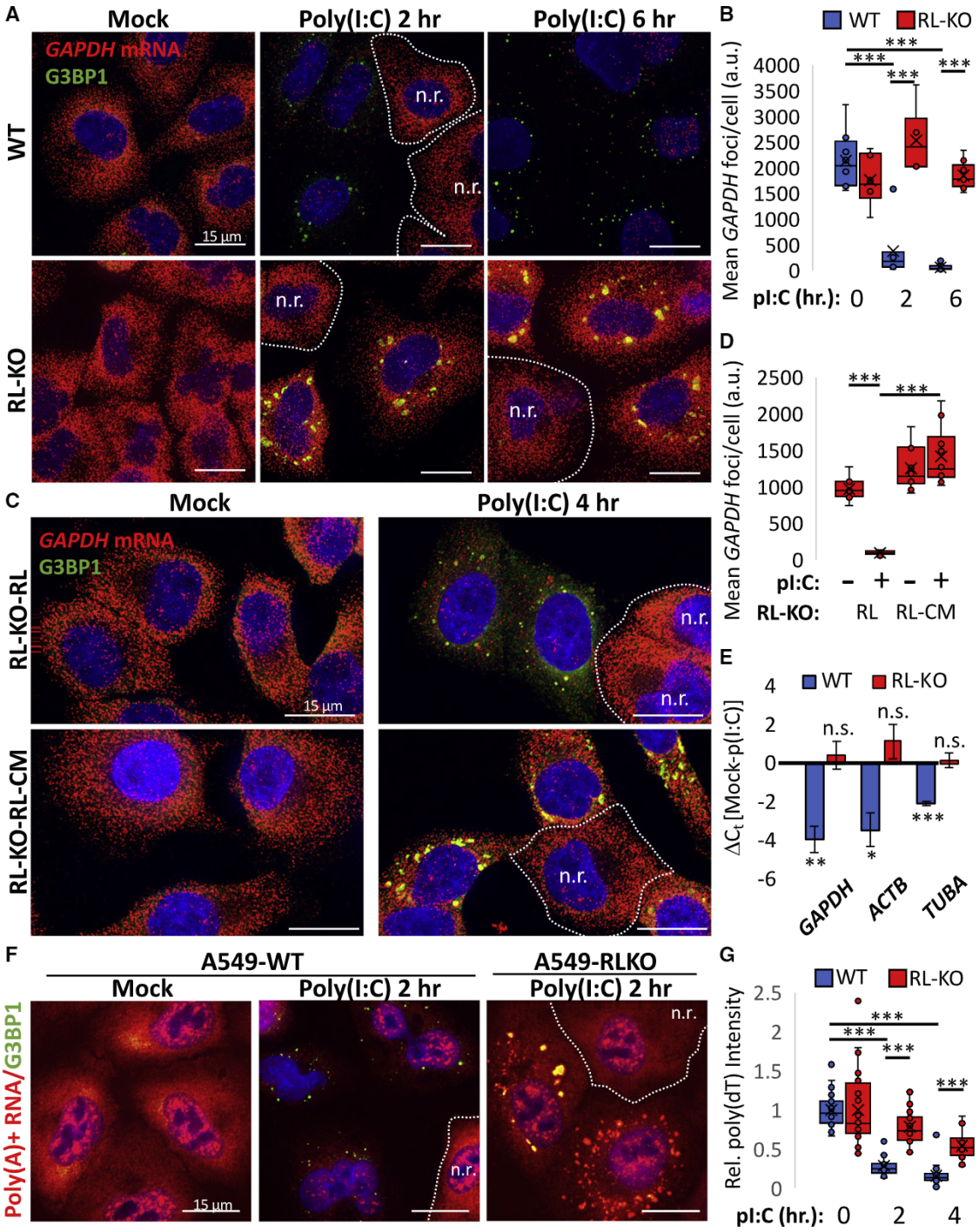

Figure 2. RNase L Promotes Widespread Turnover of mRNAs

(A) smFISH for *GAPDH* mRNA (red) in WT and RL-KO A549 cells.

(B) Quantification of *GAPDH* mRNA smFISH represented in (A).

(C) smFISH/IF for *GAPDH* mRNA and G3BP1 in RL-KO cells rescued with RNase L (RL) or RNase L-R667A (RL-CM).

(D) Quantification of *GAPDH* mRNA smFISH represented in (C).

(legend continued on next page)

present in cells that degraded the *GAPDH* mRNA. Strikingly, in cells wherein *GAPDH* mRNA had been reduced by RNase L in response to poly(I:C), cytosolic *IFN-β* mRNA was abundant (Figures 3A, S3A, and S3B). Quantification of *IFN-β* mRNA by both smFISH and quantitative reverse transcription PCR (RT-qPCR) revealed that it was induced to comparable levels between WT and RL-KO cells post-poly(I:C) (Figures 3B and 3C). These data indicate that the *IFN-β* mRNA is resistant to RNase L-mediated mRNA degradation.

We observed a similar phenomenon assaying the *IL-6* mRNA via smFISH, although there were more *IL-6* mRNAs present in the RL-KO cells (Figures S3C and S3D), which suggests the *IL-6* mRNA is only partially resistant to RNase L degradation. Consistent with this, qRT-PCR revealed that *IL-6* mRNA induction was less in WT cells as compared to RL-KO cells (Figure 3C). Similarly, the *GADD34* mRNA is induced by poly(I:C) but is reduced in an RNase L-dependent manner as assessed by qRT-PCR. Thus, there are mRNA-specific differences in resistance to RNase L degradation, even among mRNAs induced by IRF3/7.

Differential PRR Activation in Individual Cells in Response to dsRNA

Our single-cell analyses of mRNAs, RLBs, and SGs revealed an unexpected cell-to-cell variability in the response to dsRNA. For example, while the six WT cells treated with poly(I:C) in Figure 3A all showed RNase L activation, as determined by the formation of RLBs and degradation of GAPDH mRNA, only three cells strongly induced the *IFN-β* mRNA (Figure 3A, white arrows). We also observed cells that induced the *IFN-β* mRNA without activation of RNase L (Figure S3B). Similarly, in RL-KO cells, we can observe individual cells that activate PKR (as assessed by SG formation), with or without induction of the *IFN-β* mRNA (Figure 3, white and yellow arrows). We also observed RL-KO cells that induced the *IFN-β* mRNA without activation of PKR (Figure 3A, orange arrow). Interestingly, WT cells only generate RLBs and not SGs (Figure 1), indicating that PKR activation does not commonly occur without co-activation of RNase L in individual WT cells. These differences are not due to failures in transfections because cells are activating one portion of the response to dsRNA, but not other pathways. This demonstrates that individual cells respond differentially to dsRNA, which can allow multiple cellular outcomes during the dsRNA/antiviral response (see Discussion).

Genome-wide Analysis of RNase L-Mediated mRNA Degradation

To identify the RNase L-sensitive and RNase L-resistant mRNAs on a comprehensive scale, we performed high-throughput RNA sequencing on WT and RL-KO A549 cells ± poly(I:C) transfection. Standard differential expression analysis showed that few RNAs were significantly up- or downregulated between untreated WT and RL-KO cell lines (Figure S4A). In response to poly(I:C), a substantial number of RNAs significantly decreased or increased in WT cells (Figure 4A). In contrast, only a small number of RNAs significantly increased in RL-KO cells. We then normalized RNA levels to ERCC (External RNA Controls Consortium) spike-in RNAs to control for the expected gross reductions in mRNA. This was a necessary step because the number of upregulated and downregulated RNAs in WT cells post-poly(I:C), as well as the magnitude by which they changed, was overestimated and underestimated, respectively, by standard differential expression analyses (Figures S4B–S4E). We then calculated the differential in ERCC-normalized RNA levels between WT and RL-KO cells in response to poly(I:C) and plotted as a color gradient on the scatterplot of WT cells treated with or without poly(I:C) (Figure 4B; Data S1). These analyses revealed several important observations.

First, we observed that poly(I:C) transfection in WT cells led to a striking reduction in essentially all abundant mRNAs, with RNA transcripts from 6,310 genes being reduced by 2-fold or more (Figure 4B; Data S2). This was most notable for abundant mRNAs with long steady-state half-lives (Figures 4C and S4F–S4I; Tani et al., 2012), which is consistent with our RT-qPCR analysis of *GAPDH*, *actin B*, and *tubulin A* mRNAs (Figure 2E). Importantly, the decrease in these mRNAs is due to RNase L because the vast majority of abundant mRNAs did not substantially change in RL-KO cells post-poly(I:C) (Figures 4A, S4C, and S4E). Mitochondrial mRNAs (i.e., MT-ND4 and MT-ND4L) were unaffected, and in fact slightly increased in WT cells relative to RL-KO cells post-poly(I:C), effectively serving as an internal control that suggests our analyses may underestimate the level of RNase L-dependent reductions in cytosolic mRNAs (Figures 4B, S4D, and S4E). These results confirm that RNase L promotes the degradation of the majority of abundant and stable cytoplasmic mRNAs.

Second, we identified 5,101 RNA transcripts whose levels increase at least 2-fold in WT cells relative to RL-KO cells in response to post-poly(I:C) (Figure 4B, blue dots; Data S3). The majority of these RNAs are lower in abundance and have a short half-life in untreated cells (Figures 4C and S4F–S4I), which may be due to several explanations. First, RNase L may not increase the overall decay rate of these mRNAs because their decay rate is already high. Therefore, despite our use of the ERCC spike-in control, the increase in these RNAs may be a technical artifact, whereby their relative abundance is artificially inflated due to the reduction in the majority of abundant mRNAs. Second, RNase L activation may stabilize a subset of mRNAs with short half-lives. Finally, RNase L activation may promote the transcriptional induction of numerous genes.

Third, we identified constitutively expressed mRNAs (i.e., *MYC*, *SRRM2*, *STAT1*) that do not decrease in WT cells post-poly(I:C). Interestingly, STAT1 mediates interferon signaling for ISG production, and MYC is a negative regulator of IRF7 (Kim

(E) qRT-PCR quantification in WT and RL-KO A549 cells transfected with or without (Mock) poly(I:C) for 6 h. Bars represent the average C_t value differential ± SEM from at least five independent experiments.

(F) Oligo(dT) (red) and G3BP1 (green) staining of WT and RL-KO A549 cells.

(G) Quantification of mean oligo(dT) FISH signal in RLB/SG-positive cells as represented in (F). Greater than 20 cells were analyzed at the indicated times post-poly(I:C). Asterisks indicate p value <0.05 as determined by Student's t test.

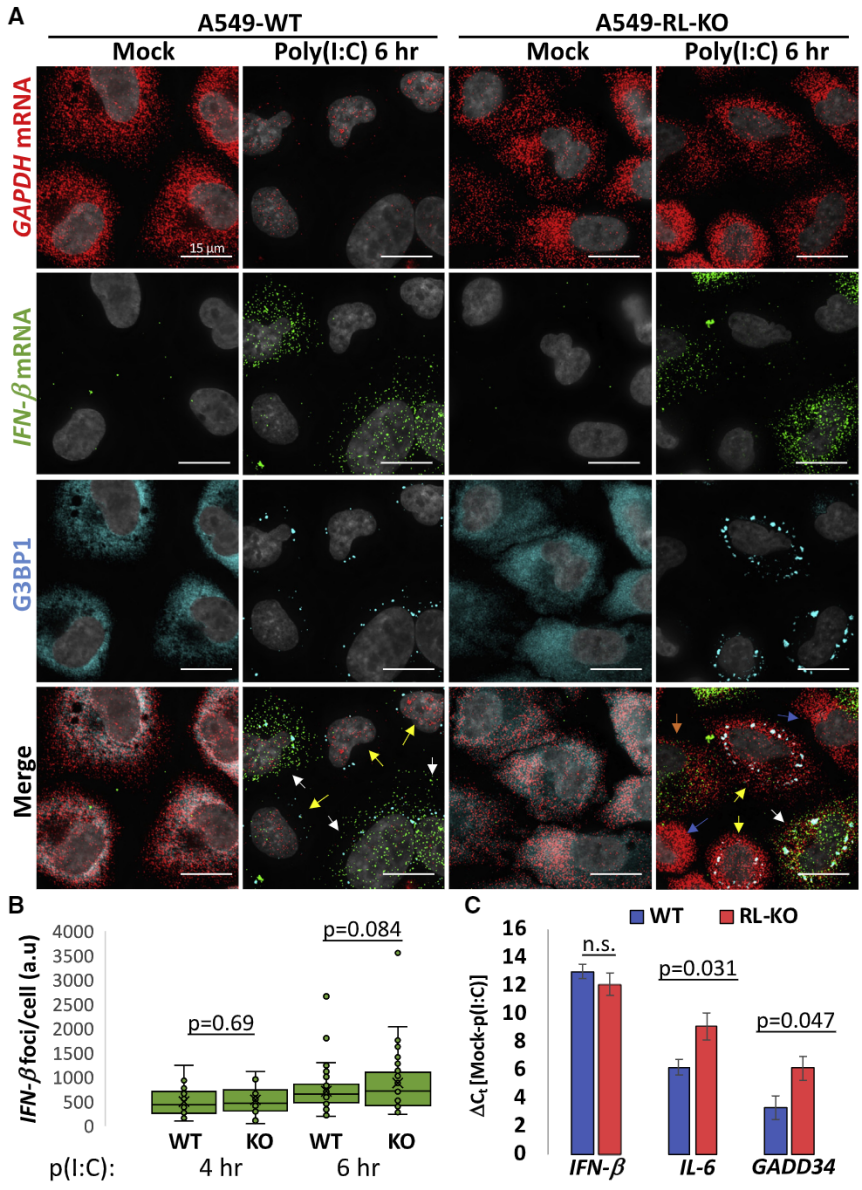

Figure 3. *IFN-β* mRNA Escapes RNase L-Mediated mRNA Turnover

(A) smFISH/IF for *IFN-β* mRNA, *GAPDH* mRNA, and G3BP1 in WT and RL-KO A549 cells. Cells that contain RLBs/SGs and *IFN-β* mRNA indicated by white arrows. Cells with RLBs/SGs without *IFN-β* mRNA are indicated by yellow arrows. Cells with *IFN-β* mRNA without RLBs/SGs are indicated by orange arrows. Cells lacking both RLBs/SGs and *IFN-β* mRNA indicated by blue arrows.

(B) Quantification of *IFN-β* mRNA smFISH in WT and RL-KO A549 cells.

(C) RT-qPCR analysis of *IFN-β*, *IL-6*, and *GADD34* mRNA expression in WT and RL-KO A549 cells 6 h post-poly(I:C). Bars represent the average C_t value ± the SEM from >5 independent experiments. Student's t test was used to determine p values.

et al., 2016). We note that *STAT1* has been shown to be induced by type I and type II interferons in some studies (Rusinova et al., 2013), and thus we cannot rule out that it is sensitive to RNase L but also transcriptionally induced. Nevertheless, these data suggest that a portion of constitutively expressed mRNAs, some of which regulate the antiviral response, also escape RNase L-mediated mRNA turnover.

Fourth, we identified a population of ~100 mRNAs that substantially increases (>4-fold) in WT and/or RL-KO cells in response to poly(I:C) (Figure 4B; Data S4). This population of mRNAs, which includes *IFN-β*, *IFIT2*, *OAS2*, *IFIH1* (*MDA5*), *DDX58* (*RIG-I*), and *IL-6*, is highly enriched for IRF3-induced mRNAs and interferon-stimulated genes (ISGs) (Figure 4D). Several of these mRNAs, such as *IFN-β*, are induced equally between WT and RL-KO cells (Figure 4B; Data S4), which is consistent with our smFISH and RT-qPCR analyses and suggests that these dsRNA-induced antiviral mRNAs escape RNase L-mediated mRNA turnover (Figure 3). Some mRNAs, such as the *IL-6* and *RAET1L* mRNAs, are induced to higher levels in the RL-KO cell line suggesting they are partially sensitive to RNase L. These data suggest there is a range of RNase L resistance among dsRNA-induced mRNAs.

The dsRNA-induced mRNAs resistant to RNase L do not have substantial differences in GC-content, 5′ UTR length, 3′ UTR length, and total transcript length of in comparison to RNase L sensitive mRNAs (Data S1), suggesting that these features may not contribute to RNase L resistance. MEME analysis of their 3′ UTRs did not identify a notable sequence motif common to all of these mRNAs, although many of these mRNAs (31%) contain AU-rich elements (AREs) (Data S4), a common motif in mRNAs encoding cytokines (Savan, 2014). Meta-analysis of CLIP studies for RBPs did not reveal a significant enrichment in association with RBPs and these mRNAs (data not shown). However, we note that many of these mRNAs are expressed at very low levels without induction by dsRNA, and the CLIP studies were not performed during dsRNA stress.

These data demonstrate that RNase L activation promotes the turnover of abundant mRNAs in response to poly(I:C), whereas highly-induced antiviral mRNAs are partially or wholly resistant to this process.

RNase L Drives Translational Repression via Bulk mRNA Turnover

The RNase L-dependent turnover of mRNAs led us to examine if this contributes to dsRNA-induced translational repression.

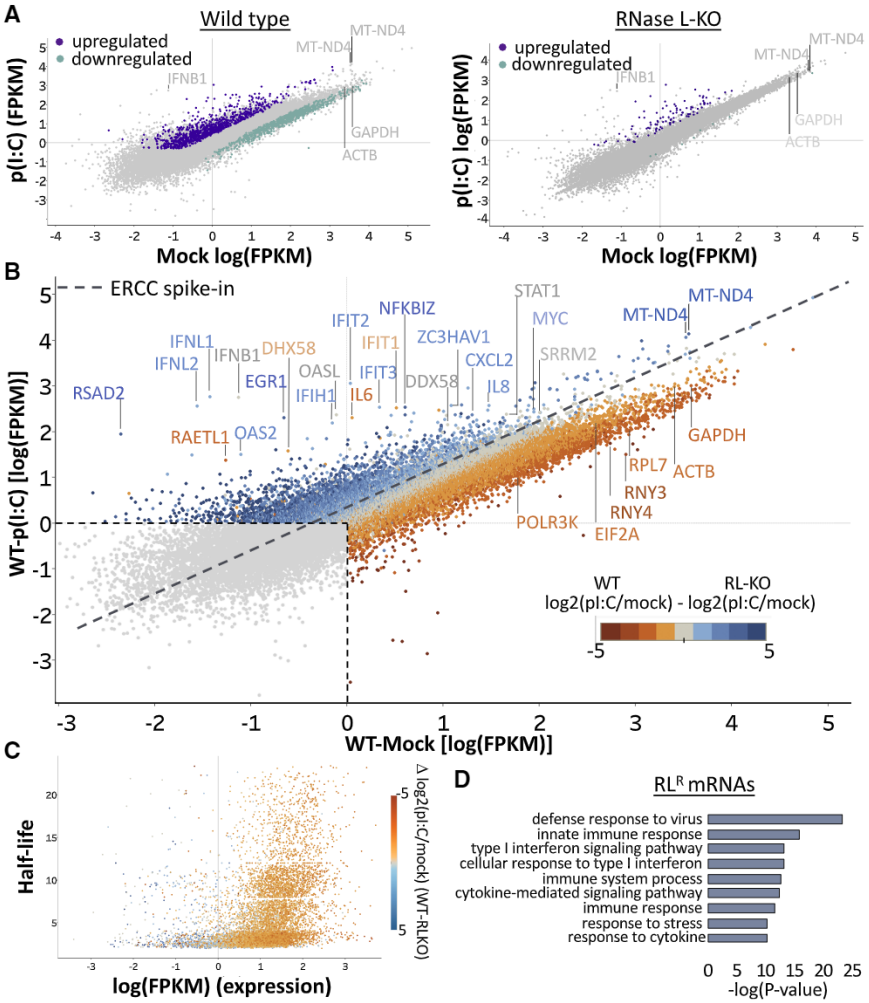

Figure 4. RNase L Regulates Global mRNA Levels during dsRNA Stress

(A) Differential expression analysis without normalization from total RNA isolated from WT or RNase L-KO A549 cells before and 6 h after poly(I:C) transfection (upregulated transcripts = fold change >2, p value <0.05; downregulated transcripts = fold change <0.5, p value <0.05).

(B) Differential expression plot of mRNAs in WT cells treated with or without poly(I:C). The linear regression of the ERCC spike-in control RNAs is represented by dashed line. The color of the dots indicates their ERCC-normalized differential expression relative to RL-KO cells transfected ± poly(I:C). Orange, RNase L-dependent decrease; blue, RNase L-dependent increase.

(C) Scatterplot depicting half-life versus expression levels (fragments per kilobase of transcript per million [FPKM]). Each transcript is color-coded by its ERCC-normalized differential expression between WT and RL-KO cells transfected ± poly(I:C).

(D) GO analysis of mRNAs that are induced in both WT and RL-KO cells post-poly(I:C) (>4-fold, FPKM >1 in either WT or RL-KO cells with poly(I:C) treatment) (Data S4).

Currently, RNase L is thought to repress translation by degrading rRNA (Wreschner et al., 1981) or by RNase L-cleaved RNAs inhibiting translation (Donovan et al., 2017), possibly by triggering phosphorylation of eIF2α by PKR, which is the primary eIF2α kinase activated by dsRNA (Dalet et al., 2015). To resolve the relative contributions of these mechanisms to RNase L-driven translational repression, we evaluated dsRNA-induced translational repression in cell lines with or without RNase L and/or PKR.

Our data argue that RNase L activity drives rapid translation repression independently of PKR in the majority of A549 cells in response to dsRNA. The key observation is that metabolic labeling of nascent proteins with either ^{35}S-labeled methionine and cysteine or puromycin revealed that both WT and PKR-KO cells strongly repressed translation by 2-h post-poly(I:C), whereas RL-KO cells maintained translation (Figures 5A, 5B, S5A, and S5B), consistent with previous analyses in A549 cells (Donovan et al., 2017).

The lack of translational repression in the RL-KO cells was surprising because some cells generate PKR-dependent SGs (Figure 1), which we hypothesized might be due to variation in the response of individual cells. Therefore, we examined translation in individual cells by IF for puromycin-labeled proteins (Schmidt et al., 2009). This analysis revealed that the RL-KO cells containing SGs in fact repressed bulk translation in response to poly(I:C), which was dependent on PKR because PKR/RL-dKO cells did not repress translation in response to poly(I:C) (Figures 5C–5F). However, <30% of the RL-KO cells repressed translation in response to poly(I:C) (Figure 5F). In contrast, >80% of the WT and PKR-KO cells underwent translational repression and showed RLB body formation with nuclear translocation of PABPC1. These data demonstrate that RNase L represses translation in the majority of A549 cells in response to dsRNA, whereas PKR represses translation in a minority of cells lacking RNase L, providing additional evidence for variation in how individual cells respond to dsRNA. Importantly, reduced puromycin-labeling was only observed in WT cells that underwent RNase L-dependent mRNA degradation (Figure 5G). This indicates that bulk mRNA degradation may significantly contribute to the RNase L-mediated translational arrest.

In addition to degrading mRNAs, RNase L could repress translation by degrading rRNA or by activating signaling pathways that trigger eIF2α phosphorylation independently of PKR. Examination of rRNA revealed it was largely intact at 2 h post-poly(I:C) when RNase L-mediated translation repression and mRNA degradation is robust (Figures 6A and S5C). Furthermore, a parallel study to ours demonstrated that cleavage of rRNA by RNase L does not reduce the ability of ribosomes to translate in extracts (Rath et al., 2019). These observations argue that rRNA degradation does not drive RNase L-driven translational

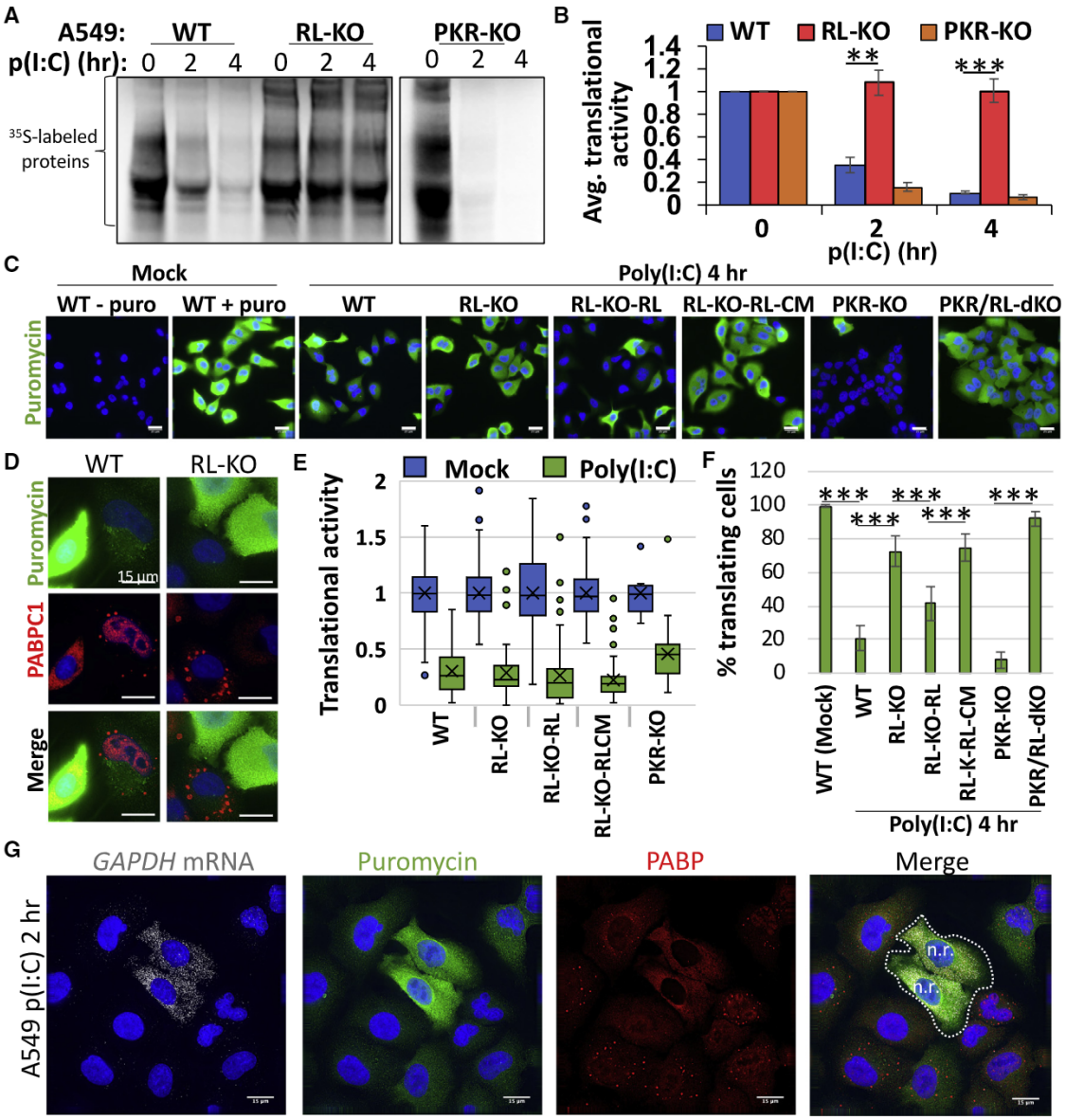

Figure 5. RNase L Drives Translational Shutoff

(A) S-35 metabolic labeling of newly synthesized proteins in WT, RL-KO, and PKR-KO A549 cells post-poly(I:C).

(B) Quantification of experiments represented in (A). Bars represent the average signal from at least two independent replicates ± SD normalized to time zero.

(C) Representative images from SUnSET puromycin-labeling (green) analysis of indicated cells lines 4 h post-poly(I:C) transfection. Dapi-stained nuclei (blue). Scale bar is 25 µm.

(D) Similar to (C) but enlarged.

(E) Quantification of the mean intensity normalized to mock-treated cells of puromycin staining in cells (between 51–176 cells analyzed for each cell line) that contain RLBs/SGs 4 h post-poly(I:C).

(F) Quantification of the percentage of cells translating (puromycin signal >80% of average signal from untreated cells) 4 h post-poly(I:C). Bars represent the average ± SD normalized to untreated cells from at least three independent replicates in which cells from at least five fields of view were analyzed.

(G) Representative image of simultaneous SUnSET puromycin-labeling (green), PABP IF (red), and GAPDH smFISH (white) in A549 cells post-poly(I:C). Cells that do not contain RLBs or do not display PABP translocation are labeled non-responsive cells (n.r.). Asterisks indicate p value <0.05 as determined by Student's t test.

repression at early times post-dsRNA, which is also supported by our analysis of IFN-β translation (see below).

Examination of eIF2α phosphorylation revealed that RNase L promotes phosphorylation of eIF2α, as p-eIF2α levels were lower (2- to 3-fold) in cells lacking RNase L activity post-poly(I:C) (Figures 6B, 6C, S5D, and S5E). This phosphorylation of eIF2α is partly independent of PKR, because PKR-KO cells also showed eIF2α phosphorylation post-poly(I:C), albeit less than in WT cells

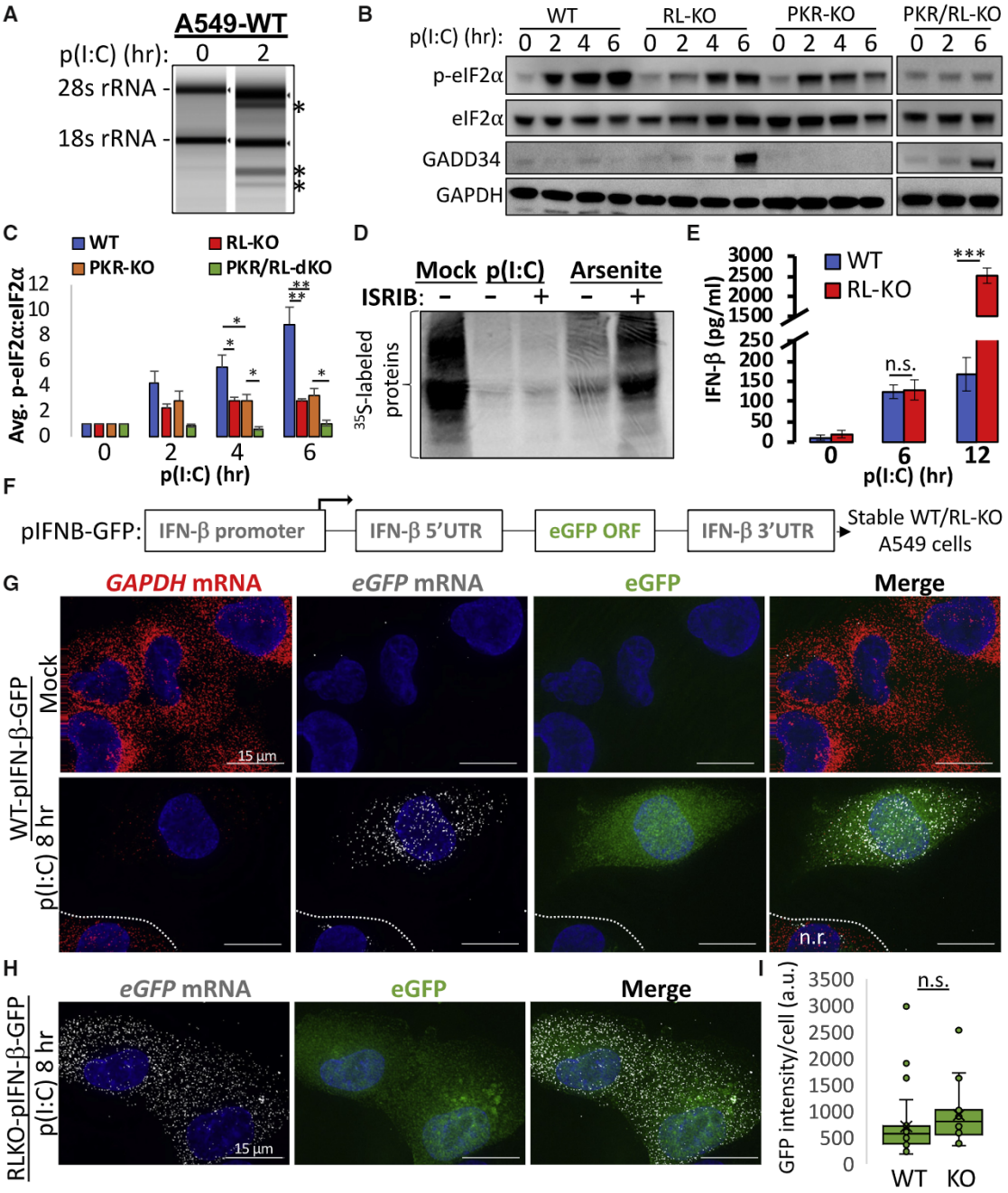

Figure 6. RNase L-Driven Translational Repression Is Independent of rRNA Degradation and p-eIF2α

(A) TapeStation analysis of the 28S and 18S rRNAs.

(B) Immunoblot analysis of eIF2α, eIF2α-P51S (p-eIF2α), GADD34, and GAPDH in indicated A549 cell lines.

(C) Quantification of the p-eIF2α:eIF2α ratio as represented in (B). Bars represent the average ratio ± SEM from independent replicates (n = 5–9).

(D) S-35 metabolic-labeling in A549 cells transfected with poly(I:C) or treated with 250 μM sodium arsenite then treated with or without ISRIB (50 nM).

(E) Quantification of IFN-β secretion from WT and RL-KO A549 via ELISA. Limit of quantification was 50 pg/mL. Bars represent average ± SD from three independent experiments. ***p value <0.001 as determined by Student's t test.

(F) Diagram of the eGFP expression vector in which *eGFP* ORF containing the *IFN-β* UTRs is driven by the *IFN-β* promoter.

(G) smFISH for *GAPDH* and *eGFP* mRNAs in A549-WT cells with the *IFN-β* promoter-eGFP vector stably incorporated. GFP fluorescence is shown.

(H) Similar to (G) but in A549-RL-KO cells.

(I) Quantification of mean eGFP intensity from at least fifteen WT and RL-KO cells as represented in (G) and (H). Asterisks indicate p value <0.05 as determined by Student's t test.

(Figures 6B, 6C, and S5F). Furthermore, this alternative mode of eIF2α phosphorylation is dependent on RNase L because eIF2α phosphorylation was abolished to background levels in PKR/RL-dKO cell lines. This suggests that RNase L activates an additional eIF2α kinase. RNase L also inhibits the induction of the GADD34 eIF2α phosphatase post-poly(I:C) (Figures 3C, 6B, and S5G), which likely promotes elevated p-eIF2α levels. Thus, RNase L activation promotes phosphorylation of eIF2α.

To determine whether RNase L-promoted phosphorylation of eIF2α contributes to RNase L-driven translational shutoff, we quantified translational activity in WT cells following transfection of poly(I:C) in the presence or absence of ISRIB, which bypasses the inhibitory effect of p-eIF2α on translation (Sidrauski et al., 2015). Strikingly, poly(I:C)-induced translational arrest was unaffected by ISRIB treatment (Figure 6D). In contrast, ISRIB derepressed sodium arsenite-induced translation arrest, which occurs through eIF2α phosphorylation. This demonstrates that phosphorylation of eIF2α is not the primary driver of rapid RNase L-mediated translational repression.

RNase L-Resistant mRNAs Continue to Translate during a dsRNA Response

The observations above argue that RNase L-mediated mRNA turnover accounts for the RNase L-dependent decrease in bulk translation. Nevertheless, it remained possible that translation is repressed by an unknown RNase L-dependent mechanism. We reasoned that if translational repression is simply due to mRNA degradation, then mRNAs that escape RNase L degradation, such as *IFN-β*, should still produce protein. Alternatively, if global translation is repressed by an unknown signaling mechanism or degradation of tRNAs, then IFN-β protein would not be produced despite the presence of the *IFN-β* mRNA.

An important observation is that WT and RL-KO cells secreted equivalent levels of IFN-β at 6 h post-poly(I:C) as measured by ELISA (Figure 6E), indicating that RNase L-driven translational repression at early times post-poly(I:C) does not negatively affect IFN-β translation and secretion. These results demonstrate that RNase L-resistant mRNAs are able to be translated at early times post-dsRNA. This argues that the translation machinery is functional and translation is simply limited by the presence of mRNAs. At 12 h post-poly(I:C), secreted IFN-β from WT cells was ~10-fold lower than from RL-KO cells (Figure 6E). This is consistent with previous findings that RNase L activity limits IFN-β secretion at later times, perhaps due to promotion of eIF2α phosphorylation, complete degradation of the translational machinery, and/or the cells entering the apoptotic pathway (Banerjee et al., 2014).

To directly demonstrate that mRNAs could be translated in cells where RNase L had degraded most cytoplasmic mRNAs, we stably transfected A549 cells with an *IFN-β* gene where the coding region was replaced with the *eGFP* ORF, referred to as $I_{5'}G_{ORF}I_{3'}$ mRNA (Figure 6F). In untreated cells, the $I_{5'}G_{ORF}I_{3'}$ mRNA and eGFP protein was essentially undetectable by smFISH and fluorescence microscopy (Figure 6G). However, transfection of poly(I:C) induced the $I_{5'}G_{ORF}I_{3'}$ mRNA in WT cells in which the majority of *GAPDH* mRNA was degraded, and those cells produced comparable, albeit slightly lower (24%), levels of GFP protein as compared to RL-KO cells 8 h post-poly(I:C) (Figure 6G,H,I). These data directly demonstrate that a cell with widespread mRNA degradation can still support translation from a transcriptionally induced mRNA that is of sufficient abundance.

ORF Sequences Can Modulate RNase L-Mediated Decay

In the above experiment, the $I_{5'}G_{ORF}I_{3'}$ mRNA levels were sufficient to produce eGFP protein during RNase L-mediated mRNA decay/translational repression (Figure 6I). However, the $I_{5'}G_{ORF}I_{3'}$ mRNA levels were 2-fold lower in WT cells in comparison to RL-KO cells 8 h post-poly(I:C), whereas endogenous *IFN-β* mRNA levels were equivalent (Figures 7A–7C and S6A). This observation suggested that the $I_{5'}G_{ORF}I_{3'}$ transcript is more sensitive to RNase L-mediated mRNA decay than the endogenous *IFN-β* mRNA even when expressed from the *IFN-β* promoter. In principle, the increased RNase L sensitivity of the $I_{5'}G_{ORF}I_{3'}$ mRNA could be because the *IFN-β* mRNA contains a protective element within its ORF, or because the *eGFP* ORF is more sensitive to RNase L cleavage.

To distinguish between these two models, we inserted the *eGFP* ORF into the *IFN-β* mRNA ($I_{5'}I{+}G_{ORF}I_{3'}$) and determined how this chimeric mRNA was affected by RNase L activation. We observed that the $I_{5'}I{+}G_{ORF}I_{3'}$ was expressed at ~4-fold lower levels in WT cells as compared to RNase L-KO cells (Figures 7A–7C), indicating that addition of the *eGFP* ORF to the *IFN-β* mRNA sensitized it to RNase L. This demonstrates that the *eGFP* ORF contains elements that confer RNase L sensitivity to the *IFN-β* mRNA. This observation also argues that the *IFN-β* mRNA does not contain a dominant protective element that limits RNase L-mediated degradation.

Because the ORFs of *eGFP* and *IFN-β* affected RNase L degradation differentially, we examined if ribosome association with these mRNAs modulated RNase L-mediated mRNA degradation by treating cells with puromycin, which will release ribosomes from mRNAs, or with emetine or cycloheximide, which trap elongating ribosomes on mRNAs. We observed that the RNase L resistance of *IFN-β* mRNA, as well as the RNase L sensitivity of *GAPDH*, $I_{5'}G_{ORF}I_{3'}$, and $I_{5'}I{+}G_{ORF}I_{3'}$ mRNAs, were unaffected by the chemical perturbation of translation (Figures S6A–S6H). We interpret this data to suggest that the translation status of an mRNA is not a major determinant of its sensitivity or resistance to RNase L.

The partial escape of the $I_{5'}G_{ORF}I_{3'}$ mRNAs from RNase L led us to assess the contribution of the *IFN-β* UTRs in protecting the eGFP ORF from RNase L. To test this, we swapped the *IFN-β* 5′ and 3′ UTRs in the $I_{5'}G_{ORF}I_{3'}$ for the 5′ and 3′ UTRs of the pcDNA3.1 plasmid (termed $V_{5'}G_{ORF}V_{3'}$) and examined expression in WT and RL-KO 8 h post-poly(I:C). We observed that the $V_{5'}G_{ORF}V_{3'}$ and $I_{5'}G_{ORF}I_{3'}$ mRNAs were expressed to similar levels and both were reduced to a similar degree in WT cells as compared to RL-KO cells (Figures 7A–7C). This argues that, at least in this context, the 5′ and 3′ UTRs of the *IFN-β* mRNA do not confer RNase L resistance to the *eGFP* mRNA.

RNase L-Promoted Transcription of *IFN-β* Promotes Escape from RNase L-Mediated mRNA Decay

The partial escape of the $I_{5'}G_{ORF}I_{3'}$ and $V_{5'}G_{ORF}V_{3'}$ mRNAs driven by the *IFN-β* promoter from RNase L led us to investigate if transcriptional induction could contribute to mRNAs escaping

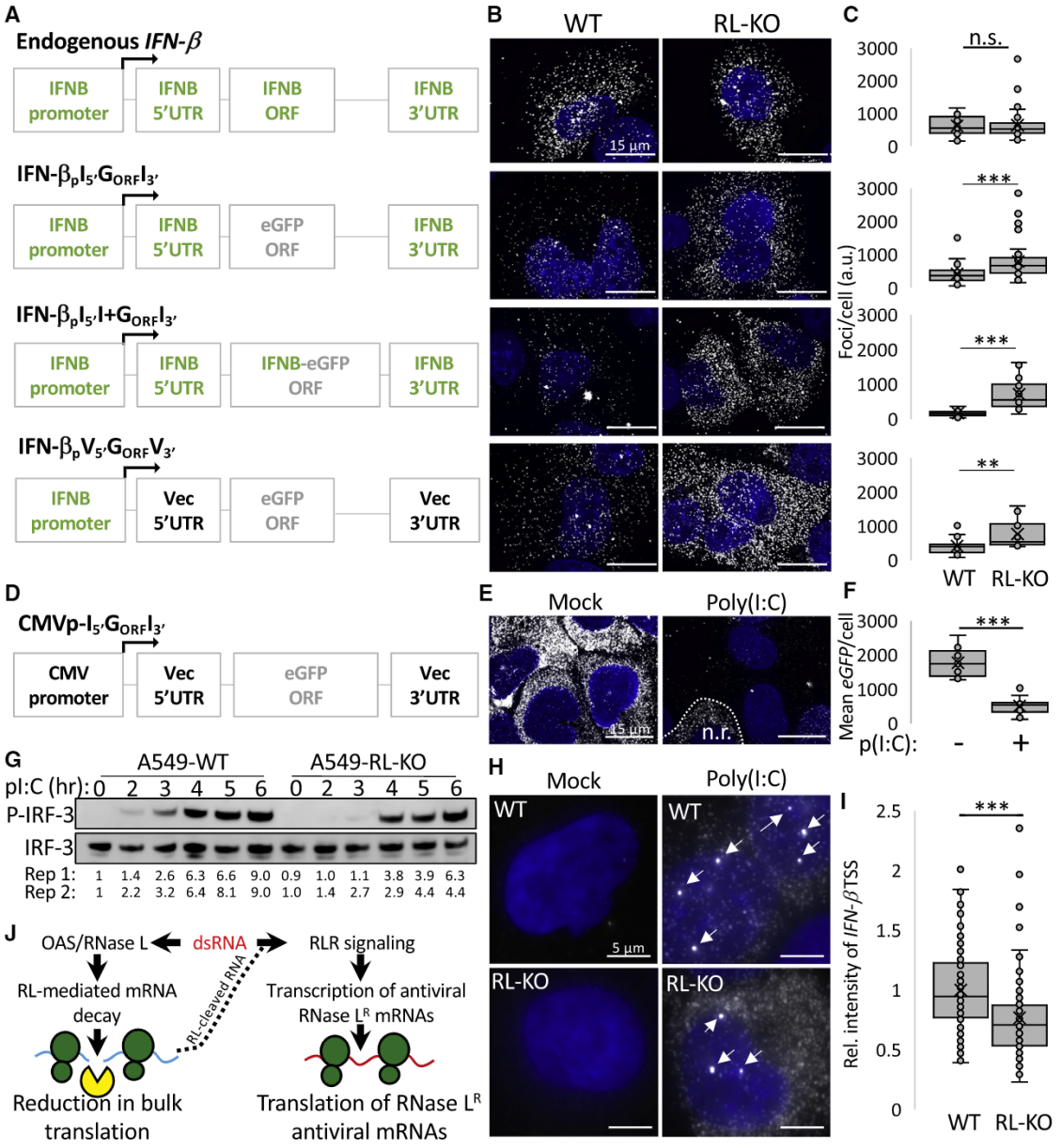

Figure 7. *IFN-β* mRNA Escapes RNase L-Mediated Decay via Resistance to RNase L and RNase L-Promoted Transcriptional Induction

(A) Diagrams of endogenous *IFN-β* gene and *eGFP* constructs driven by the *IFN-β* promoter.

(B) smFISH for *IFN-β* (top images) and *eGFP* (lower images) mRNAs from expression constructs depicted directly to the left in (A) 8 h post-poly(I:C). *IFN-β* smFISH was performed in WT and RL-KO A549 cells with the *IFN-β*$_p$*I*$_{5'}$*G*$_{ORF}$*I*$_{3'}$ construct stably incorporated.

(C) Quantification of smFISH foci per cell as represented in the images in (B) directly to the left. Between 17 and 59 cells were analyzed from each line.

(D) Diagram of CMV promoter-driven *eGFP*.

(E) smFISH for *eGFP* mRNA driven by the CMV promoter in WT cells with or without poly(I:C) transfection. smFISH for *GAPDH* mRNA and GFP fluorescence in WT and RL-KO cells is shown in Figures S7A and S7B.

(F) Quantification of eGFP smFISH represented in (E).

(G) Immunoblot analysis of p-IRF3 (rep 1). Normalized p-IRF3 band intensity from two experiments are shown below.

(H) *IFN-β* smFISH from non-deconvolved images. Arrows mark high-intensity RNase A-sensitive and actinomycin D-sensitive foci consistent with nascent transcripts at *IFN-β* loci (Figures S7D–S7F).

(I) Quantification of the relative intensity of *IFN-β* TSS in WT and RL-KO cells represented in (H). Between 111–138 foci were analyzed from three independent experiments. Asterisks indicate p value <0.05 as determined by Student's t test.

(J) Model of RNase L-mediated regulation of translation via mRNA degradation escaped by antiviral mRNAs.

RNase L degradation. To examine this, we compared the RNase L sensitivity of the $V_{5'}G_{ORF}V_{3'}$ mRNA constitutively expressed from the CMV promoter (Figure 7D), which is not induced by dsRNA, to the same mRNA expressed from the *IFN-β* promoter. We observed that the CMV-driven $V_{5'}G_{ORF}V_{3'}$ mRNA significantly decreased in WT but not RL-KO cells post-poly(I:C) (Figures 7E, 7F, and S7A–S7C), indicating that the $V_{5'}G_{ORF}V_{3'}$ mRNA is sensitive to RNase L to a degree similar to *GAPDH* mRNA. In contrast, the *eGFP* mRNAs driven by the *IFN-β* promoter increased in abundance post-poly(I:C). Furthermore, the relative RNase L-dependent reduction of the $V_{5'}G_{ORF}V_3$ mRNA was 2-fold less than when driven from the *IFN-β* promoter in comparison to the CMV promoter. These observations suggest that transcriptional activation from the *IFN-β* promoter counteracts RNase L-mediated decay of the *eGFP* mRNAs.

One possibility is that RNase L activation promotes induction of the *IFN-β* promoter to offset increased mRNA decay (Malathi et al., 2007). Indeed, we observed higher (30%) p-IRF3 levels in WT cells in comparison to RL-KO cells (Figure 7G), and the average intensity of nascent transcripts at the *IFN-β* transcriptional start site (TSS) was higher (24%) in WT cells in comparison to RL-KO cells as assessed by smFISH (Figures 7H, 7I, and S7D–S7F). These data indicate that RNase L promotes transcription of antiviral mRNAs and are consistent with mathematical modeling suggesting that transcriptional induction with a stable positive feedback activator can promote escape from RNase L activation (Rath et al., 2019). Thus, these data combined support that RNase L-promoted transcriptional induction coupled with elements/structures of the *IFN-β* mRNA that resist RNase L cleavage are sufficient for the *IFN-β* mRNA to effectively escape RNase L-mediated mRNA decay (Figure 7J).

DISCUSSION

Our studies demonstrate that RNase L leads to rapid and widespread degradation of the majority of abundant cytoplasmic mRNAs in response to dsRNA (Figures 1E, 2, and 4A-4C). Consistent with these findings, a related study demonstrated that RNase L increases decay rates of large numbers of mRNAs in response to dsRNA (Rath et al., 2019). However, despite the promiscuous nature of RNase L degradation, some mRNAs fully, or partially, escape RNase L-mediated mRNA degradation. For example, the *IFN-β* mRNA is expressed at similar levels in WT and RL-KO cells post-poly(I:C) by both qRT-PCR and smFISH (Figure 3), indicating that RNase L does not affect the levels of this mRNA. Indeed, from our RNA sequencing (RNA-seq) analyses, we identify numerous mRNAs that fully, or partially, escape RNase L-mediated mRNA degradation (Figure 4B). Importantly, many of these mRNAs encode for dsRNA-induced antiviral proteins and cytokines (Figure 4D).

Multiple mechanisms presumably contribute to the observation that mRNAs are differentially affected by RNase L. First, the magnitude of an mRNA being reduced by RNase L depends on its normal mRNA decay rate relative to the rate of RNase L-mediated decay. This, in part, explains the observation that stable mRNAs are more strongly reduced by RNase L in comparison to unstable mRNAs (Figures 4C and 4F–4I). Because many RNase L-resistant antiviral mRNAs contain destabilizing elements, such as AREs (Data S4), RNase L-mediated mRNA decay would be expected to have less of an impact on their overall decay rate.

Second, some mRNAs may have evolved sequence and/or structural compositions that resist RNase L cleavage or specific elements that directly modulate RNase L activity. Notably, a conserved RNA structure in poliovirus inhibits RNase L activation (Han et al., 2007; Townsend et al., 2008), and selective pressure by RNase L has been proposed to account for the reduced frequency of UA and UU dinucleotides in HCV RNA (Washenberger et al., 2007). Similar to the latter mechanism, we observed that the RNase L-sensitive *eGFP* ORF is sufficient to sensitize the *IFN-β* mRNA to RNase L (Figures 7A–7F and S7A–S7C). This effect appears to be independent of ribosome association and translational status, because we did not observe differences in RNase L sensitivity of *GAPDH*, *IFN-β*, $I_{5'}I+G_{ORF}I_3$, and $I_{5'}G_{ORF}I_3$ mRNAs upon chemical perturbation of translation (Figures S6A–S6H). These observations suggest that RNase L targeting of mRNA is not strongly associated with ribosomes, which leads to two important implications. First, bulk mRNAs can be degraded by RNase L in cells undergoing translational repression via PKR-mediated phosphorylation of eIF2α. Second, antiviral mRNAs that are resistant to RNase L cleavage would be permitted to be translated without being targeted for degradation. Combined, these observations argue that the *IFN-β* mRNA may have evolved in sequence composition/structure to reduce cleavage by RNase L. Indeed, inherent differences in RNase L-mediated mRNA degradation rates are observed in cell-free systems (Rath et al., 2015). Because mRNAs typically fold well *in vitro* in a manner that reflects the *in vivo* structure (Beaudoin et al., 2018), this suggests that mRNAs can be differentially degraded by RNase L simply based on their structure and the accessibility of RNase L cleavage sites.

Finally, transcriptional rates of IRF3-induced mRNAs may outpace RNase L-mediated mRNA decay rates of these mRNAs. Indeed, expression of RNase L-sensitive *eGFP* mRNA from the *IFN-β* promoter is sufficient to allow partial escape from RNase L (Figures 7A–7G and S7A–S7C). Furthermore, our studies and previous studies support that RNase L promotes IRF3 phosphorylation and transcriptional induction of *IFN-β* (Figures 7G–7I and S7D–S7F) (Malathi et al., 2007), which could compensate for increased mRNA decay. Consistent with this, kinetic analyses of the dsRNA response and RNase L-mediated mRNA decay links increased stability of antiviral mRNAs to transcriptional positive feedback of the interferon response, whereby RNase L-resistant molecules (i.e., IFN proteins or p-STAT protein) protect non-resistant molecules (i.e., mRNAs) from RNase L (Rath et al., 2019). In this view, a combination of inherent mRNA instability, structural resistance to RNase L cleavage, and transcriptional induction promoted by RNase L and/or IFN signaling likely contributes to the ability of antiviral mRNAs to escape RNase L-mediated mRNA decay.

Several of our observations argue that one consequence of RNase L-mediated mRNA degradation is host shutoff of translation. First, we observed that RNase L catalytic activity represses translation by 2 h post-dsRNA (Figures 5A, 5B, S5A, and S5B), when rRNA is largely intact (Figures 6A and S5C), but bulk mRNA levels are substantially reduced (Figures 2 and S2G). Second, RNase L-dependent bulk translational repression is

unaffected by ISRIB or knockout of PKR (Figures 5A, 5B, 6D, S5A, and S5B), indicating RNase L-driven translational repression occurs independently of eIF2α phosphorylation. Third, reduced puromycin labeling of cells correlates with RNase L-dependent loss of *GAPDH* mRNA and PABP translocation (Figure 5G). Finally, because the *IFN-β* mRNA escapes RNase L-driven mRNA turnover and IFN-β protein is produced at similar levels in WT and RL-KO cells prior to robust rRNA degradation (Figures 3 and 6E), this demonstrates that the presence of a stable mRNA is sufficient to produce protein, and therefore the translation machinery is functional. Consistent with this latter finding, a related study demonstrated that antiviral cytokines are produced during RNase L-mediated translational arrest (Chitrakar et al., 2019). Combined, these observations reveal a new mode of RNase L-driven translational repression that occurs via bulk mRNA turnover and permits the translation of key RNase L-resistant antiviral mRNAs, such as the *IFN-β* mRNA (Figure 7J).

A second consequence of robust mRNA degradation by RNase L is inhibition of SG assembly concurrent with the assembly of small punctuate SG-like bodies (RLBs) and PABPC1 translocation to the nucleus (Figure 1). Interestingly, PABPC1 translocation and small punctate SGs that resemble RLBs, which are both hallmarks of RNase L activation revealed in our studies, have been observed during infection of numerous and diverse viruses (Lee and Glaunsinger, 2009; Kumar and Glaunsinger, 2010; Gray et al., 2015; Montero et al., 2008; Dobrikova et al., 2010; Borah et al., 2011; Fros et al., 2012; Khaperskyy et al., 2014). However, in contrast to previous studies (Dalet et al., 2017), we did not observe strong enrichment of antiviral mRNAs in SGs or RLBs (Figures 3 and S3), and the presence or absence of SGs and RLBs did not appear to markedly affect IFN-β production at early times post-poly(I:C) (Figure 6E). Therefore, an important focus of future work will be to determine the functions of RNase L-mediated inhibition of SGs, RLBs, and RNase L-mediated PABP translocation during the dsRNA/antiviral response.

We suggest that the activation of RNase L and widespread degradation of host mRNAs acts in concert with other aspects of the dsRNA response. Specifically, the sensing of dsRNA by PRRs leads to (1) the activation of IRF3, which promotes the transcription of antiviral genes such as type I interferons; (2) the activation of RNase L, which initiates widespread degradation of both host and viral RNAs; (3) PKR- and RNase L-mediated promotion of eIF2α phosphorylation changing the specificity of translation initiation; and (4) Inhibition of canonical translation re-initiation via RNase L-mediated downregulation of the GADD34 p-eIF2α phosphatase (Figures 6B and S5G). In the context of these four outcomes, the majority of IRF3 induced genes appear to be resistant to RNase L-mediated mRNA turnover, and this allows for their selective translation. Thus, RNase L-mediated degradation of cellular mRNAs leads to reprogramming of the produced proteins to only those mRNAs resistant to RNase L activity.

Strikingly, by examining single cells, we observe that different aspects of the cellular response to dsRNA can be triggered independently in individual cells. We observe numerous instances where RNase L activation and PKR activation are uncoupled from induction of IRF3 targets, such as the *IFN-β* mRNA (Figures 3A, S3A, and S3B). The ability to independently activate different arms of the cellular response to dsRNA allows cells to modulate their transcriptional and translational output, as well as to determine whether to enter apoptosis. An important aspect of future work will be to determine the additional inputs that affect the independent activation of these pathways and how those affect the cellular response to viral infection.

STAR★METHODS

Detailed methods are provided in the online version of this paper and include the following:

- KEY RESOURCES TABLE
- LEAD CONTACT AND MATERIALS AVAILABILITY
- EXPERIMENTAL MODEL AND SUBJECT DETAILS
  - Cell lines
- METHOD DETAILS
  - Plasmids
  - Antibodies
  - Generation of knockout cell lines
  - Generation of Lentiviral particles
  - Generation of stable cell lines
  - Immunoblot analyses
  - Sequential immunofluorescence and single molecule FISH
  - Microscopy and Image Analysis
  - RT-qPCR
  - Metabolic labeling of newly synthesized proteins
  - IFN-β ELISA
  - High-throughput RNA sequencing
- QUANTIFICATION AND STATISTICAL ANALYSIS
- DATA AND CODE AVAILABILITY

SUPPLEMENTAL INFORMATION

Supplemental Information can be found online at https://doi.org/10.1016/j.molcel.2019.07.029.

ACKNOWLEDGMENTS

The authors would like to thank Dr. Christopher Sullivan for plasmid reagents and the A549 cell line. We thank Dr. Nancy Kedersha for the U-2 OS cell line. We thank Dr. Susan Weiss for the A549 PKR-KO cell line. Image analysis was performed at the BioFrontiers Advanced Light Microscopy Core. The Imaris sofware package was supported by NIH 1S10RR026680-01A1. Research reported in this publication was supported by the National Institute of Allergy and Infectious Diseases of the NIH (F32AI145112) and funds from HHMI.

AUTHOR CONTRIBUTIONS

J.M.B. and R.P. conceived the project. J.M.B., S.L.M., and T.M. performed experiments. J.M.B., S.L.M., T.M., and R.P. reviewed and interpreted the data. J.M.B. and R.P. wrote the manuscript.

DECLARATION OF INTERESTS

The authors declare no competing interests.

Received: February 20, 2019
Revised: June 13, 2019
Accepted: July 18, 2019
Published: September 4, 2019

REFERENCES

Anders, S., Pyl, P.T., and Huber, W. (2015). HTSeq—a Python framework to work with high-throughput sequencing data. Bioinformatics *31*, 166–169.

Andersen, J.B., Mazan-Mamczarz, K., Zhan, M., Gorospe, M., and Hassel, B.A. (2009). Ribosomal protein mRNAs are primary targets of regulation in RNase-L-induced senescence. RNA Biol. *6*, 305–315.

Bailey, T.L., Boden, M., Buske, F.A., Frith, M., Grant, C.E., Clementi, L., Ren, J., Li, W.W., and Noble, W.S. (2009). MEME SUITE: tools for motif discovery and searching. Nucleic Acids Res. *37*, W202-8.

Bakheet, T., Hitti, E., and Khabar, K.S.A. (2018). ARED-Plus: an updated and expanded database of AU-rich element-containing mRNAs and pre-mRNAs. Nucleic Acids Res. *46* (D1), D218–D220.

Banerjee, S., Chakrabarti, A., Jha, B.K., Weiss, S.R., and Silverman, R.H. (2014). Cell-type-specific effects of RNase L on viral induction of beta interferon. MBio *5*, e00856-14.

Beaudoin, J.D., Novoa, E.M., Vejnar, C.E., Yartseva, V., Takacs, C.M., Kellis, M., and Giraldez, A.J. (2018). Analyses of mRNA structure dynamics identify embryonic gene regulatory programs. Nat. Struct. Mol. Biol. *25*, 677–686.

Bolger, A.M., Lohse, M., and Usadel, B. (2014). Trimmomatic: a flexible trimmer for Illumina sequence data. Bioinformatics *30*, 2114–2120.

Borah, S., Darricarrère, N., Darnell, A., Myoung, J., and Steitz, J.A. (2011). A viral nuclear noncoding RNA binds re-localized poly(A) binding protein and is required for late KSHV gene expression. PLoS Pathog. *7*, e1002300.

Brennan-Laun, S.E., Ezelle, H.J., Li, X.-L., and Hassel, B.A. (2014). RNase-L control of cellular mRNAs: roles in biologic functions and mechanisms of substrate targeting. J. Interferon Cytokine Res. *34*, 275–288.

Burke, J.M., Kincaid, R.P., Nottingham, R.M., Lambowitz, A.M., and Sullivan, C.S. (2016). DUSP11 activity on triphosphorylated transcripts promotes Argonaute association with noncanonical viral microRNAs and regulates steady-state levels of cellular noncoding RNAs. Genes Dev. *30*, 2076–2092.

Chakrabarti, A., Jha, B.K., and Silverman, R.H. (2011). New insights into the role of RNase L in innate immunity. J. Interferon Cytokine Res. *31*, 49–57.

Chitrakar, A., Rath, S., Donovan, J., Demarest, K., Li, Y., Sridhar, R.R., Weiss, S.R., Kotenko, S.V., Wingreen, N.S., and Korennykh, A. (2019). Real-time 2-5A kinetics suggest that interferons β and λ evade global arrest of translation by RNase L. Proc. Natl. Acad. Sci. USA *116*, 2103–2111.

Dalet, A., Gatti, E., and Pierre, P. (2015). Integration of PKR-dependent translation inhibition with innate immunity is required for a coordinated anti-viral response. FEBS Lett. *589*, 1539–1545.

Dalet, A., Argüello, R.J., Combes, A., Spinelli, L., Jaeger, S., Fallet, M., Vu Manh, T.P., Mendes, A., Perego, J., Reverendo, M., et al. (2017). Protein synthesis inhibition and GADD34 control IFN-β heterogeneous expression in response to dsRNA. EMBO J. *36*, 761–782.

Dobrikova, E., Shveygert, M., Walters, R., and Gromeier, M. (2010). Herpes simplex virus proteins ICP27 and UL47 associate with polyadenylate-binding protein and control its subcellular distribution. J. Virol. *84*, 270–279.

Donovan, J., Rath, S., Kolet-Mandrikov, D., and Korennykh, A. (2017). Rapid RNase L-driven arrest of protein synthesis in the dsRNA response without degradation of translation machinery. RNA *23*, 1660–1671.

Fros, J.J., Domeradzka, N.E., Baggen, J., Geertsema, C., Flipse, J., Vlak, J.M., and Pijlman, G.P. (2012). Chikungunya virus nsP3 blocks stress granule assembly by recruitment of G3BP into cytoplasmic foci. J. Virol. *86*, 10873–10879.

García, M.A., Gil, J., Ventoso, I., Guerra, S., Domingo, E., Rivas, C., and Esteban, M. (2006). Impact of protein kinase PKR in cell biology: from antiviral to antiproliferative action. Microbiol. Mol. Biol. Rev. *70*, 1032–1060.

Gaspar, I., Wippich, F., and Ephrussi, A. (2017). Enzymatic production of single-molecule FISH and RNA capture probes. RNA *23*, 1582–1591.

Gray, N.K., Hrabálková, L., Scanlon, J.P., and Smith, R.W. (2015). Poly(A)-binding proteins and mRNA localization: who rules the roost? Biochem. Soc. Trans. *43*, 1277–1284.

Grivennikov, S.I., Greten, F.R., and Karin, M. (2010). Immunity, inflammation, and cancer. Cell *140*, 883–899.

Han, J.Q., Townsend, H.L., Jha, B.K., Paranjape, J.M., Silverman, R.H., and Barton, D.J. (2007). A phylogenetically conserved RNA structure in the poliovirus open reading frame inhibits the antiviral endoribonuclease RNase L. J. Virol. *81*, 5561–5572.

Iordanov, M.S., Paranjape, J.M., Zhou, A., Wong, J., Williams, B.R.G., Meurs, E.F., Silverman, R.H., and Magun, B.E. (2000). Activation of p38 mitogen-activated protein kinase and c-Jun $NH_{(2)}$-terminal kinase by double-stranded RNA and encephalomyocarditis virus: involvement of RNase L, protein kinase R, and alternative pathways. Mol. Cell. Biol. *20*, 617–627.

Ivashkiv, L.B., and Donlin, L.T. (2014). Regulation of type I interferon responses. Nat. Rev. Immunol. *14*, 36–49.

Jensen, S., and Thomsen, A.R. (2012). Sensing of RNA viruses: a review of innate immune receptors involved in recognizing RNA virus invasion. J. Virol. *86*, 2900–2910.

Kedersha, N., Panas, M.D., Achorn, C.A., Lyons, S., Tisdale, S., Hickman, T., Thomas, M., Lieberman, J., McInerney, G.M., Ivanov, P., and Anderson, P. (2016). G3BP-Caprin1-USP10 complexes mediate stress granule condensation and associate with 40S subunits. J. Cell Biol. *212*, 845–860.

Khaperskyy, D.A., Emara, M.M., Johnston, B.P., Anderson, P., Hatchette, T.F., and McCormick, C. (2014). Influenza a virus host shutoff disables antiviral stress-induced translation arrest. PLoS Pathog. *10*, e1004217.

Khong, A., Matheny, T., Jain, S., Mitchell, S.F., Wheeler, J.R., and Parker, R. (2017). The stress granule transcriptome reveals principles of mRNA accumulation in stress granules. Mol. Cell *68*, 808–820.e5.

Kim, D., Pertea, G., Trapnell, C., Pimentel, H., Kelley, R., and Salzberg, S.L. (2013). TopHat2: accurate alignment of transcriptomes in the presence of insertions, deletions and gene fusions. Genome Biol. *14*, R36.

Kim, T.W., Hong, S., Lin, Y., Murat, E., Joo, H., Kim, T., Pascual, V., and Liu, Y.J. (2016). Transcriptional Repression of IFN Regulatory Factor 7 by MYC Is Critical for Type I IFN Production in Human Plasmacytoid Dendritic Cells. J. Immunol. *197*, 3348–3359.

Kinsella, R.J., Kähäri, A., Haider, S., Zamora, J., Proctor, G., Spudich, G., Almeida-King, J., Staines, D., Derwent, P., Kerhornou, A., et al. (2011). Ensembl BioMarts: a hub for data retrieval across taxonomic space. Database (Oxford) *2011*, bar030.

Krug, L., Chatterjee, N., Borges-Monroy, R., Hearn, S., Liao, W.-W., Morrill, K., Prazak, L., Rozhkov, N., Theodorou, D., Hammell, M., and Dubnau, J. (2017). Retrotransposon activation contributes to neurodegeneration in a *Drosophila* TDP-43 model of ALS. PLoS Genet. *13*, e1006635.

Kumar, G.R., and Glaunsinger, B.A. (2010). Nuclear import of cytoplasmic poly(A) binding protein restricts gene expression via hyperadenylation and nuclear retention of mRNA. Mol. Cell. Biol. *30*, 4996–5008.

Langmead, B., and Salzberg, S.L. (2012). Fast gapped-read alignment with Bowtie 2. Nat. Methods *9*, 357–359.

Lee, Y.J., and Glaunsinger, B.A. (2009). Aberrant herpesvirus-induced polyadenylation correlates with cellular messenger RNA destruction. PLoS Biol. *7*, e1000107.

Li, Y., Banerjee, S., Goldstein, S.A., Dong, B., Gaughan, C., Rath, S., Donovan, J., Korennykh, A., Silverman, R.H., and Weiss, S.R. (2017). Ribonuclease L mediates the cell-lethal phenotype of double-stranded RNA editing enzyme ADAR1 deficiency in a human cell line. eLife *6*, e25687.

Liddicoat, B.J., Piskol, R., Chalk, A.M., Ramaswami, G., Higuchi, M., Hartner, J.C., Li, J.B., Seeburg, P.H., and Walkley, C.R. (2015). RNA editing by ADAR1 prevents MDA5 sensing of endogenous dsRNA as nonself. Science *349*, 1115–1120.

Lloyd, R.E. (2013). Regulation of stress granules and P-bodies during RNA virus infection. Wiley Interdiscip. Rev. RNA *4*, 317–331.

Malathi, K., Dong, B., Gale, M., Jr., and Silverman, R.H. (2007). Small self-RNA generated by RNase L amplifies antiviral innate immunity. Nature *448*, 816–819.

Mi, H., Huang, X., Muruganujan, A., Tang, H., Mills, C., Kang, D., and Thomas, P.D. (2017). PANTHER version 11: expanded annotation data from Gene Ontology and Reactome pathways, and data analysis tool enhancements. Nucleic Acids Res. *45* (D1), D183–D189.

Montero, H., Rojas, M., Arias, C.F., and López, S. (2008). Rotavirus infection induces the phosphorylation of eIF2α but prevents the formation of stress granules. J. Virol. *82*, 1496–1504.

Moon, S.L., and Parker, R. (2018). *EIF2B2* mutations in vanishing white matter disease hypersuppress translation and delay recovery during the integrated stress response. RNA *24*, 841–852.

Onomoto, K., Jogi, M., Yoo, J.-S., Narita, R., Morimoto, S., Takemura, A., Sambhara, S., Kawaguchi, A., Osari, S., Nagata, K., et al. (2012). Critical role of an antiviral stress granule containing RIG-I and PKR in viral detection and innate immunity. PLoS ONE *7*, e43031.

Pestal, K., Funk, C.C., Snyder, J.M., Price, N.D., Treuting, P.M., and Stetson, D.B. (2015). Isoforms of the RNA editing enzyme ADAR1 independently control nucleic acid sensor MDA5-driven autoimmunity and multi-organ development. Immunity *43*, 933–944.

Rath, S., Donovan, J., Whitney, G., Chitrakar, A., Wang, W., and Korennykh, A. (2015). Human RNase L tunes gene expression by selectively destabilizing the microRNA-regulated transcriptome. Proc. Natl. Acad. Sci. USA *112*, 15916–15921.

Rath, S., Prangley, E., Donovan, J., Demarest, K., Wingreen, N., Meir, Y., and Korennykh, A. (2019). 2-5A-Mediated mRNA Decay and Transcription Act in Concert to Reprogram Protein Synthesis during dsRNA Response. bioRxi. https://doi.org/10.1101/484675.

Reineke, L.C., Dougherty, J.D., Pierre, P., and Lloyd, R.E. (2012). Large G3BP-induced granules trigger eIF2α phosphorylation. Mol. Biol. Cell *23*, 3499–3510.

Rusinova, I., Forster, S., Yu, S., Kannan, A., Masse, M., Cumming, H., Chapman, R., and Hertzog, P.J. (2013). Interferome v2.0: an updated database of annotated interferon-regulated genes. Nucleic Acids Res. *41*, D1040–D1046.

Saldi, T.K., Ash, P.E., Wilson, G., Gonzales, P., Garrido-Lecca, A., Roberts, C.M., Dostal, V., Gendron, T.F., Stein, L.D., Blumenthal, T., et al. (2014). TDP-1, the Caenorhabditis elegans ortholog of TDP-43, limits the accumulation of double-stranded RNA. EMBO J. *33*, 2947–2966.

Savan, R. (2014). Post-transcriptional regulation of interferons and their signaling pathways. J. Interferon Cytokine Res. *34*, 318–329.

Schindelin, J., Arganda-Carreras, I., Frise, E., Kaynig, V., Longair, M., Pietzsch, T., Preibisch, S., Rueden, C., Saalfeld, S., Schmid, B., et al. (2012). Fiji: an open-source platform for biological-image analysis. Nat. Methods *9*, 676–682.

Schmidt, E.K., Clavarino, G., Ceppi, M., and Pierre, P. (2009). SUnSET, a nonradioactive method to monitor protein synthesis. Nat. Methods *6*, 275–277.

Sidrauski, C., McGeachy, A.M., Ingolia, N.T., and Walter, P. (2015). The small molecule ISRIB reverses the effects of eIF2α phosphorylation on translation and stress granule assembly. eLife *4*, e05033.

Tani, H., Mizutani, R., Salam, K.A., Tano, K., Ijiri, K., Wakamatsu, A., Isogai, T., Suzuki, Y., and Akimitsu, N. (2012). Genome-wide determination of RNA stability reveals hundreds of short-lived noncoding transcripts in mammals. Genome Res. *22*, 947–956.

Townsend, H.L., Jha, B.K., Silverman, R.H., and Barton, D.J. (2008). A putative loop E motif and an H-H kissing loop interaction are conserved and functional features in a group C enterovirus RNA that inhibits ribonuclease L. RNA Biol. *5*, 263–272.

Trapnell, C., Hendrickson, D.G., Sauvageau, M., Goff, L., Rinn, J.L., and Pachter, L. (2013). Differential analysis of gene regulation at transcript resolution with RNA-seq. Nat. Biotechnol. *31*, 46–53.

Van Treeck, B., Protter, D.S.W., Matheny, T., Khong, A., Link, C.D., and Parker, R. (2018). RNA self-assembly contributes to stress granule formation and defining the stress granule transcriptome. Proc. Natl. Acad. Sci. USA *115*, 2734–2739.

Waldner, H. (2009). The role of innate immune responses in autoimmune disease development. Autoimmun. Rev. *8*, 400–404.

Washenberger, C.L., Han, J.Q., Kechris, K.J., Jha, B.K., Silverman, R.H., and Barton, D.J. (2007). Hepatitis C virus RNA: dinucleotide frequencies and cleavage by RNase L. Virus Res. *130*, 85–95.

Wreschner, D.H., James, T.C., Silverman, R.H., and Kerr, I.M. (1981). Ribosomal RNA cleavage, nuclease activation and 2-5A(ppp(A2'p)nA) in interferon-treated cells. Nucleic Acids Res. *9*, 1571–1581.

Yang, Y.C., Di, C., Hu, B., Zhou, M., Liu, Y., Song, N., Li, Y., Umetsu, J., and Lu, Z.J. (2015). CLIPdb: a CLIP-seq database for protein-RNA interactions. BMC Genomics *16*, 51.

Yoo, J.-S., Takahasi, K., Ng, C.S., Ouda, R., Onomoto, K., Yoneyama, M., Lai, J.C., Lattmann, S., Nagamine, Y., Matsui, T., et al. (2014). DHX36 enhances RIG-I signaling by facilitating PKR-mediated antiviral stress granule formation. PLoS Pathog. *10*, e1004012.

Zhou, A., Paranjape, J., Brown, T.L., Nie, H., Naik, S., Dong, B., Chang, A., Trapp, B., Fairchild, R., Colmenares, C., and Silverman, R.H. (1997). Interferon action and apoptosis are defective in mice devoid of 2′,5′-oligoadenylate-dependent RNase L. EMBO J. *16*, 6355–6363.

STAR★METHODS

KEY RESOURCES TABLE

REAGENT or RESOURCE	SOURCE	IDENTIFIER
Antibodies		
Mouse anti-RNase L Antibody 2E9	Novus Biologicals	NB100-351; RRID:AB_10081934
Rabbit anti-IRF3	Abcam	ab25950; RRID:AB_2126991
Rabbit anti-phospho-IRF3 (Ser396) (D601M)	Cell signaling Technology	29047S; RRID:AB_2773013
Mouse monoclonal anti-G3BP antibody	Abcam	ab56574; RRID:AB_941699
Rabbit anti-EIF2S1 (Phospho S51- eIF2α)	Abcam	ab32157; RRID:AB_732117
Rabbit anti-eIF2α	Cell Signaling Technology	CST9722S; RRID:AB_10695409
Mouse monoclonal anti-FLAG	Sigma Aldrich	F1804; RRID:AB_262044
Rabbit anti-GAPDH	Cell Signaling Technology	2118L; RRID:AB_561053
Rabbit anti-PKR	Cell Signaling Technology	12297S; RRID:AB_2665515
Rabbit polyclonal anti-PABP	Abcam	ab21060; RRID:AB_777008
Goat anti-mouse IgG H&L FITC	Abcam	ab97022; RRID:AB_10681023
Goat anti-rabbit IgG H&L Alexa Fluor 647	Abcam	ab150079; RRID:AB_2722623
Anti-rabbit IgG, HRP-linked antibody	Cell Signaling Technology	7074S; RRID:AB_2099233
Anti-mouse IgG, HRP-linked antibody	Cell Signaling Technology	7076S; RRID:AB_330924
Anti-puromycin	MilliporeSigma	MABE343; RRID:AB_2566826
Chemicals, Peptides, and Recombinant Proteins		
Sodium (meta)arsenite	Sigma-Aldrich	S7400
Poly(I:C) HMW	InvivoGen	tlrl-pic
Lipofectamine 2000	Thermo Fisher Scientific	11668027
Trizol LS reagent	Thermo Fisher Scientific	10296-028
Blasticidine S hydrochloride	Sigma-Aldrich	15205
ddUTP-Atto633	Axxora	JBS-NU-1619-633
terminal deoxynucleotidyl transferase	Thermo Fisher Scientific	EP0161
Polybrene	Millipore	TR-1003-G
iQ SYBR green master mix	Bio-Rad	1708880
Super script III reverse transcriptase	Thermo Fisher Scientific	18080085
Critical Commercial Assays		
IFN beta human ELISA kit	Thermo Fisher Scientific	414101
Deposited Data		
Raw and processed sequencing files	This study	GEO: GSE124144
Unprocessed image files, Mendeley Dataset DOI	This study	https://doi.org/10.17632/khkbgmkt4d.1
Experimental Models: Cell Lines		
A549 cells	Burke et al., 2016	N/A
U-2 OS cells	Kedersha et al., 2016	N/A
A549-PKR-KO cells	Li et al., 2017	N/A
HEK293T cells	Burke et al., 2016	N/A
Oligonucleotides		
Stellaris FISH Probes Quasar 570 Dye GAPDH	Biosearch Technologies	SMF-2026-1
Custom IFNB1, IL-6, eGFP Stellaris FISH Probes	Biosearch Technologies	Data S6
Oligo d(T)30-Cy3	IDT	N/A
qRT-PCR primers	IDT	Data S6
NORAD and AHANK smFISH probes	Biosearch Technologies	Khong et al., 2017

(*Continued on next page*)

Continued

REAGENT or RESOURCE	SOURCE	IDENTIFIER
Recombinant DNA		
px458 Cas9 vector	Addgene	48138
Software and Algorithms		
Trimmomatic 0.32	Bolger et al., 2014	http://www.usadellab.org/cms/?page=trimmomatic
HTSeq	Anders et al., 2015	https://htseq.readthedocs.io/en/release_0.9.1/
Bowtie2 2.0.2	Langmead and Salzberg, 2012	http://bowtie-bio.sourceforge.net/bowtie2/index.shtml
Tophat 2.0.6	Kim et al., 2013	http://ccb.jhu.edu/software/tophat/index.shtml
Cuffdiff 2.2.1	Trapnell et al., 2013	http://cole-trapnell-lab.github.io/cufflinks/cuffdiff/
Imaris Image Analysis Software 8.4.1	Bitplane	https://imaris.oxinst.com
ARED	Bakheet et al., 2018	https://brp.kfshrc.edu.sa/ared/Home/BasicSearch
Gene Ontology Consortium enrichment analysis	Mi et al., 2017	http://www.geneontology.org/

LEAD CONTACT AND MATERIALS AVAILABILITY

Information and requests for resources and reagents should be directed to and will be fulfilled by the Lead Contact, Roy Parker (roy.parker@colorado.edu).

EXPERIMENTAL MODEL AND SUBJECT DETAILS

Cell lines

A549, U-2 OS, and A549-PKR-KO cell lines were provided by Dr. Christopher Sullivan, Dr. Nancy Kedersha, and Dr. Susan Weiss, respectively. Cells were maintained at 5% CO_2 and 37°C in Dulbecco's modified eagle' medium (DMEM) supplemented with fetal bovine serum (FBS; 10% v/v) and penicillin/streptomycin (1% v/v). Cells were routinely tested for mycoplasma contamination by the cell culture core facility and were negative for mycoplasma contamination throughout the study. Cells were transfected with poly(I:C) HMW (InvivoGen: tlrl-pic) using 3-ul of lipofectamine 2000 (Thermo Fisher Scientific) per 1-ug or poly(I:C).

METHOD DETAILS

Plasmids

To generate the 3xflag-tagged RNase L expression vectors used for transient transfections, the RNase L and RNase L-R667 coding sequences were tagged with 3x-flag encoding sequence via PCR amplification from the pLenti-CMV-RNase L and pLenti-RNase L-R667A vectors using the RL-3xFlag-Kpn1/Xho1 primers (Data S5) and Phusion polymerase (New England BioLabs). The PCR amplicons were digested with Kpn1 and Xho1 and ligated into the *Kpn1/Xho1* sites of pcDNA3.1-puro using T4 DNA ligase (New England BioLabs). To generate pLenti-EF1-Blast lentiviral genomes encoding RNase L and RNase L-R667A, the RNase L and RNase L-R667A coding sequences were N-terminally-tagged with 3x-flag tag via PCR amplification expression vectors using RL-3x-flag-fusion primers (RL_sen_3x_FLAG, RL_sen_kpn1_kozak_flag, and RL_anti_EcoN1) (Data S5) and inserted into the *Xho1/EcoN1* sites of the pLenti-EF1-Blast vector using In-Fusion (Clontech). The pVSV-G, pRSV-Rev, and pMDLg/pRRE plasmids were a gift from Dr. Sabrina Spencer. The px458 Cas9 vector (Addgene: 48138) was used to generate knockout cell lines. The CRISPR/Cas9 guide RNAs were designed using the Integrated DNA Technologies (IDT) CRISPR guide target design tool. Overlapping oligos (RL sgRNA 1 sense an RL sgRNA 1 antisense (Data S5) were annealed in T4 DNA ligase buffer and ligated into the *Bbs1* sites in px458 using T4 DNA ligase. To generate the pIFNB1-eGFP chimera plasmids, the pcDNA3.1-puromycin plasmid was digested with BglII and Xba1, which removed the CMV promoter. The eGFP ORF and IFNB-GFP ORF chimeras were generated by a gblock (IDT, Data S5) encoding the IFN-B promoter, either the eGFP ORF or IFNB1-eGFP chimeric ORF, and the IFNB UTRs. These were fused into the pcDNA3.1-puromycin vector at the *bglII* and *xba1* sites using in-fusion cloning (Clontech). A *xho1*site was included between the eGFP ORF and IFNB1-3′UTR to allow for manipulation of the vector as needed. To generate the pIFNB1-eGFP-Vector UTR chimera, a gblock encoding the IFNB1 promoter with the pcDNA3.1+ vector 5′ UTR that overlapped with the 5′end of the eGFP ORF (Data S5), a PCR amplicon from the pLJM1-eGFP plasmid of the eGFP ORF overlapping with the 5′-UTR and 3′-UTRs of pcDNA3.1 at the 5′- and 3′ ends, respectively, was fused into the pcDNA3.1-puromycin vector at the *bglII* and *xba1* sites using in-fusion cloning (Clontech). To generate the CMV-driven eGFP construct, the eGFP ORF PCR amplicon was fused into the Nhe1/Xho1sites of pcDNA3.1. Plasmids were sequence verified via sanger sequencing (Quintarabio or Genewiz).

Antibodies

Mouse anti-RNase L Antibody 2E9 (Novus Biologicals: NB100-351) was use at 1:1500 for immunoblot analyses. Rabbit anti-IRF3 (Abcam: ab25950) was used at 1:1000 for IB analysis. Rabbit anti-phospho-IRF3 (Ser396) (D601M) (Cell signaling Technology: 29047S) was used at 1:1000 for IB analysis. Mouse monoclonal anti-G3BP antibody (Abcam: ab56574) was used at 1:500 for IFA and 1:1000 for IB analyses. Rabbit anti-EIF2S1 (Phospho S51- eIF2α) monoclonal antibody (Abcam: ab32157) was used at 1:500 for IB analysis. Rabbit anti-eIF2α (Cell Signaling Technology: CST9722S) was used at 1:1000 for IB analysis. Mouse monoclonal anti-FLAG (Sigma Aldrich: F1804) was used at 1:1000 for IB analysis. Rabbit anti-GAPDH (Cell Signaling Technology: 2118L) was used at 1:2000 for IB analysis. Rabbit anti-PKR (Cell Signaling Technology: 12297S) was used at 1:1000 for IB analysis. Rabbit polyclonal anti-PABP antibody (Abcam: ab21060) was used at 1:500 for IFA. Goat anti-mouse IgG H&L FITC (Abcam: ab97022) was used at 1:1000 for IFA. Goat anti-rabbit IgG H&L Alexa Fluor 647 (Abcam: ab150079) was used at 1:1000 for IFA. Anti-rabbit IgG, HRP-linked antibody (Cell Signaling Technology: 7074S) was used at 1:3000 for IB analysis. Anti-mouse IgG, HRP-linked antibody (Cell Signaling Technology: 7076S) was used at 1:10,000 for IB analysis. Anti-puromycin (MilliporeSigma: MABE343) was used at 1:1000 for SUnSET analyses.

Generation of knockout cell lines

To generate RNase L knockout A549 and U-2 OS lines, cells (T-25 flask; 70% confluent) were co-transfected with 2-ug of px458-RL and 200-ng of pcDNA3.1-puro using 6-ul of Lipofectamine 2000 (Thermo Fisher Scientific) according to manufacturer's instructions. Twenty-four hours post-transfection after Cas9-GFP expression was observed via fluorescent microscopy, the medium was replaced with medium containing 2ug/ml of puromycin. Selective medium was replaced 3 days post-transfection. Five days post-transfection, selective growth medium was replaced with normal growth medium. When cells became 80% confluent, cells were serial diluted and plated on 15-cm dishes. Individual colonies were isolated, propagated, and screened via immunoblot analysis.

Generation of Lentiviral particles

To generate the RNase L and RNase L-R667A lentiviral particles, HEK293T cells (15-cm dish; 80% confluent) were co-transfected with either 11.7-ug of pLenti-EF1-RNase L-blast and pLenti-EF1-3xflag-RNase L-R667A-blast, 3.5-ug of pVSV-G, 2.9-ug of pRSV-Rev, and 5.6-ug of pMDLg-pRRE using 100-ul of lipofectamine 2000. Medium was replaced 6 hours post-transfection. Medium was collected at twenty-four and forty-eight hours post-transfection and filter-sterilized with a 0.45-um filter.

Generation of stable cell lines

To reconstitute A549-RL-KO cells with either 3xflag-RNase L or 3xflag-RNase L-R667A, A549-RL-KO cells were seeded in T-25 flask. When 80% confluent, cells were incubated for 1 hour with 1 mL of either 3xflag-RNase L or 3xflag-RNase L-R667A lentiviral particles containing 10-ug of polybrene with periodic rocking. Normal medium was then added to the flask and incubated for twenty-four hours. Medium was removed 24 hours post-transduction and replaced with selective growth medium containing 10-ug/ml of Blasticidine S hydrochloride (Sigma-Aldrich). Selective medium was changed every three days. After one-week, selective medium was replaced with normal growth medium. Expression of RNase L was confirmed via immunoblot analysis. To generate the stable eGFP/IFNB chimera lines, 1-ug of each plasmid was linearized with pvuII, purified, and then transfected into cells using lipofectamine 2000. Forty-eight hours later, cells were passaged into medium containing 2-ug/ml of puromycin, and cells were maintained in selective medium. To generate cell lines with stable incorporation of the *IFN-β /eGFP* chimeric constructs, plasmids were linearized with Pvu1, purified, and 1-ug was transfected into cells (T-25 Flask; 50% confluent) using lipofectamine 2000. Forty-eight hours later, cells were passage into selective medium containing 2-ug/ml of puromycin. Cells were maintained in selective media.

Immunoblot analyses

To screen and confirm for knockout or reconstitution of proteins, cells were lysed in SDS solution (1% SDS, 2% β-mercaptoethanol) by boiling for 10 min followed by 1 min of vortexing. Equal volumes of lysates were fractionated on 4%–12% Bis-Tris Protein gels (Thermo Fisher Scientific) in MOPS buffer and transferred to nitrocellulose membrane (GE Healthcare). Membranes were blocked in 5% BSA in TBST. Membranes were then incubated with primary antibodies for 2 hours at room temperature or overnight at 4°C. After washing, membranes were incubated with HRP-linked anti-rabbit IgG or anti-mouse IgG secondary antibodies for 1 hour at room temperature. After washing, membranes were incubated with ECL substrates (Thermo Fisher Scientific: 32106) for 1-5 minutes. Membranes were then stripped using Restore western blot stripping buffer (Thermo Fisher Scientific: 21059) and re-blocked with 5% BSA in TBST. Membranes were then incubated with anti-GAPDH, washed, incubated with HRP-linked anti-mouse antibody, washed, and incubated in ECL substrate. For quantitation of p-eIF2α, cells were seeded in 12-well format. Cells were transfected with 250-ng of poly(I:C) and cell lysates were collected at indicated time post-transfection. A fifth of the lysate (12-ul/60-ul) was fractionated on 4%–12% Bis-Tris Protein gels in MOPS buffer and transferred to nitrocellulose membrane. Membranes were blocked in 5% MILK in TBST. Membranes were then incubated with rabbit anti-EIF2S1 (Phospho S51- eIF2α) antibodies overnight at 4°C. After washing, membranes were incubated with HRP-linked anti-rabbit antibody for 1 hour at room temperature. After washing, membranes were incubated with SuperSignal West Femto Maximum Sensitivity ECL substrate (Thermo Fisher Scientific: 34095) for 1-5 minutes. Membranes were stripped and re-probed using with rabbit anti-eIF2α, washed, incubated with HRP-linked anti-rabbit antibody for 1 hour at room temperature, washed, incubated with SuperSignal West Femto Maximum Sensitivity ECL substrate for

1-5 minutes. Photographs of membranes were taken using ImageQuant LAS 4000 (GE Healthcare) and analyzed using ImageJ with Fiji plug-in. For quantification of western blots, average band signal was determined using the measure function in imageJ.

Sequential immunofluorescence and single molecule FISH

Sequential immunofluorescence and smFISH was performed following manufacturer's protocol (https://biosearchassets.blob.core.windows.net/assets/bti_custom_stellaris_immunofluorescence_seq_protocol.pdf). Ship ready GAPDH smFISH probes labeled with Quasar 570 Dye were purchased from Stellaris. Custom AHNAK and NORAD smFISH probes labeled with Quasar 670 dye were designed and purchased from Stellaris and are described in Khong et al. (2017). Custom IFNB1, eGFP, and IL-6 smFISH probes (Data S6) were designed using Stellaris smFISH probe designer (Biosearch Technologies) available online at https://www.biosearchtech.com/stellaris-designer. Reverse complement DNA oligos were purchased from IDT. The IFNB1 smFISH probes were labeled with Atto-633 using ddUTP-Atto633 (Axxora: JBS-NU-1619-633) and terminal deoxynucleotidyl transferase (Thermo Fisher Scientific: EP0161) as described in Gaspar et al. (2017). Oligo d(T)30-Cy3 were purchased from IDT.

Microscopy and Image Analysis

Immunofluorescence and smFISH with DAPI staining were imaged using a wide field DeltaVision Elite microscope with a 100X objective using a PCO Edge sCMOS camera. For IFA, 10 Z sections at 0.3 um/section were taken for each image. For IFA/smFISH, 15 Z planes at 0.2 um/section were taken for each image. Deconvoluted images were processed using ImageJ with FIJI plugin. Z-planes were stacked and minimum and maximum display values were set in ImageJ for each channel to properly view fluorescence. Quantification of SGs was determined using Imaris Image Analysis Software (Bitplane) (University of Colorado-Boulder, BioFrontiers Advanced Light Microscopy Core). Live cell imaging was performed using a Nikon Spinning Disk Confocal microscope outfitted with an environmental chamber with O_2, CO_2, temperature, and humidity control (University of Colorado-Boulder, BioFrontiers Advanced Light Microscopy Core). All images were acquired using a 2x Andor Ultra 888 EMCCD camera.

RT-qPCR

WT and RL-KO A549 cells (12-well; 60% confluent) were transfected with or without poly(I:C). Six hours post-transfection, RNA was extracted, treated with DNase I (NEB) for 15 minutes, and re-purified via ethanol (75%) sodium acetate (0.3M) precipitation, and re-suspended in 15-ul of water. Equal volumes (400-ng of WT RNA) were then reverse transcribed using super script III reverse transcriptase (Thermo Fisher Scientific) and polydT$_{(20)}$ primer (Integrated DNA Technologies). cDNA was diluted to 100-ul. 2-ul of cDNA was added to qPCR reaction containing iQ SYBR green master mix (Bio-Rad) and 10-pmol of gene-specific primers, which are listed in Data S5. Reactions were run in duplicate or triplicate (technical replicates) on CFX96 qPCR machine (Bio-Rad) using standard two-step cycle. PCR fragment sizes were confirmed by ethidium bromide staining and RT- controls were included to demonstrate that amplification was from cDNA and not gDNA.

Metabolic labeling of newly synthesized proteins

Wild-type, RNase L knockout or PKR knockout A549 cells were transfected with poly(I:C) as described above. S35 metabolic labeling of nascent proteins was performed as described in Moon and Parker (2018). Briefly, cells were incubated with ^{35}S labeled met and cys (EXPRE35S35S Protein Labeling Mix, PerkinElmer) in labeling medium (DMEM lacking met and cys (Sigma Aldrich) supplemented with 10% dialyzed FBS (Sigma Aldrich), glutaMAX (GIBCO) and 1% streptomycin/penicillin) for 30 minutes at two- and four- hours post-transfection following a 30 minute incubation in labeling medium to deplete intracellular amino acid stores. Cells were harvested in NP-40 lysis buffer with protease and phosphatase inhibitors (Cell Signaling Technologies), lysed and equal volumes of lysate run on NuPAGE 4%–12% Bis-Tris protein gels (Thermo Fisher Scientific). Gels were exposed to phosphor screens and imaged on a typhoon FLA 9500 phosphorimager. The average relative translation activity was determined using ImageJ (Fiji) (Schindelin et al., 2012) to quantify total lane intensity for each sample from 2-3 independent experiments.

SUnSET was performed as described by Schmidt et al. (2009). Briefly, puromycin (10 ug/ml) was added to cells 10 minutes prior to fixing or harvesting lysates. For IF of puro-labeled cells, cells were imaged on 60X objective. Between 5 and 10 fields of view were imaged. The fluorescent intensity of puromycin labeling of individual cells was measured using fiji software.

IFN-β ELISA

WT and RL-KO A549 cells (6-well format, 1 mL or medium, 70% confluency) were transfected with poly(I:C). At six- and twelve- hours post-poly(I:C), 50-ul of medium was removed from well and immediately assayed via ELISA using IFN beta human ELISA kit (Thermo Fisher Scientific; 414101) using manufacturer's instructions. Time zero was taken by removing 50-ul of medium prior to poly(I:C) transfection.

High-throughput RNA sequencing

WT and RL-KO A549 cells (100-mm dish, 60% confluent) were transfected with or without 500-ng/ml of poly(I:C). Three independent replicates were performed. Total RNA was isolated six hours post-transfection. The ERCC spike-in was added according to manufacturer's instructions and RNA libraries were prepared by the BioFrontiers Sequencing Core at CU Boulder. Libraries were sequenced on Illumina NextSeq 500. Read quality was assessed using fastqc. Illumina adaptors were trimmed using Trimmomatic

0.32 in paired and (PE) mode (Bolger et al., 2014). An index genome was acquired from GENCODE (Release 19 GRCh37.p13). Reads were aligned using Tophat (version 2.0.6) and Bowtie2 (version 2.0.2) and the following parameters:–b2 –fast –microexon-search (Kim et al., 2013; Langmead and Salzberg, 2012). Differential expression analysis was performed using Cuffdiff (version 2.2.1) with the default parameters (Trapnell et al., 2013). Gene ontology biological processes were derived from Gene Ontology Consortium enrichment analysis (Mi et al., 2017) (http://geneontology.org/). MEME analyses were performed using MEME suite (Bailey et al., 2009). Meta-analysis of CLIP sites were derived from Yang et al. (2015). Ensembl Biomart was used for retrieval of transcript characterization (Kinsella et al., 2011). Au-rich elements were predicted using ARED (https://brp.kfshrc.edu.sa/ared/Home/BasicSearch) (Bakheet et al., 2018).

QUANTIFICATION AND STATISTICAL ANALYSIS

Student's t test was used to determine statistical significance. The exact value of n, which either represents independent experiments or individual cells, for each analysis can be found in the figure legends. On graphs, * indicates p value < 0.05, ** indicates p value < 0.005, and *** indicates p value < 0.001 as determined by Student's t test.

DATA AND CODE AVAILABILITY

Raw sequencing data are available for download GEO: GSE124144. Unprocessed images for microscopy and western blot images are deposited in the Mendeley database (https://doi.org/10.17632/khkbgmkt4d.1)